A conceptual Investigation of Turbidity Current Trigger from Alongshelf Current-supported Turbidity Currents

Celalettin E. Ozdemir[1,2,3*]

Liangyi Yue[4]

Haq Murad Nazari[1]

George Xue[2,3,5]

Samuel J. Bentley[3,6]

Shuo Yang[1]

Sayed O. Hofioni[1]

Robert Forney[5]

Saber Aradpour[1]

[1]Civil and Environmental Engineering, Louisiana State University, Baton Rouge LA 70803

[2]Center for Computation and Technology, Louisiana State University, Baton Rouge LA 70803

[3]Coastal Studies Institute, Louisiana State University, Baton Rouge LA 70803

[4]Civil and Environmental Engineering, Stanford University, Stanford CA 94305

[5]Department of Oceanography and Coastal Sciences, Louisiana State University, Baton Rouge LA 70803

[6]Department of Geology and Geophysics, Louisiana State University, Baton Rouge LA 70803

*3240L Patrick Taylor Hall, Civil and Environmental Engineering, Louisiana State University, Baton Rouge LA 70803

Key Points:

- A time-dependent depth-integrated advection model for suspended sediment concentration is developed for ACSTCs.
- Parametric limits that delineate along-shelf current-supported turbidity currents from self-driven turbidity currents are quantified.
- Settling flux, stratification, and the nonlinear interaction between entrainment and cross-shelf gravity force govern the suspension amount.

Corresponding author: Celalettin E. Ozdemir, cozdemir@lsu.edu

Abstract

Wave- and current-supported turbidity currents (WCSTCs) are one of the sediment delivery mechanisms from the inner shelf to the shelf break. Therefore, they play a significant role in the global cycles of geo-chemically important particulate matter. Recent observations suggest that WCSTCs can transform into self-driven turbidity currents close to the continental margin. However, little is known regarding the critical conditions that grow self-driven turbidity currents on WCSTCs. This is in part due to the knowledge gaps in the dynamics of WCSTCs regarding the role of density stratification. Especially the effect of sediment entrainment, and the parameters thereof, on density stratification and the amount of sediment suspension, has been overlooked. To this end, this study revisits the existing theoretical framework for a simplified WCSTC, in which waves are absent, i.e., alongshelf current-supported turbidity current (ACSTC). A depth-integrated advection model is developed for suspended sediment concentration. The analyses of the model, which are verified by turbulence-resolving simulations, indicate that the amount of suspended sediment load is regulated by the equilibrium among density stratification, positive feedback between entrainment and cross-shelf gravity force, and settling flux dissociated with density stratification. It is also found that critical density stratification is not a necessary condition for equilibrium. A quantitative relation is developed for the critical conditions for self-driven turbidity currents, which is a function of bed shear stress, entrainment parameters, bed slope, and sediment settling velocity. In addition, the suspended sediment load is analytically estimated from the model developed.

Plain Language Summary

Turbidity currents are responsible for the rapid displacement of sediments to the deep ocean. Their triggering mechanisms can be numerous, but recent observations suggest that some of the turbidity currents originate from slowly moving turbidities driven by currents and waves, also known as wave- and current-supported turbidity currents. To identify the parametric limits of the transition mentioned, the existing theoretical frame-

work for slowly moving turbidity currents is re-appraised, and the amount of sediments that can be carried by currents parallel to the shore is analytically evaluated. A parametric limit for the occurrence of fast-moving self-driven turbidity currents is developed.

1 Introduction

1.1 Motivation

Transport of river-borne sediments across the continental shelves to the continental margin is key to sediment source-to-sink and thus the global cycles of geochemically important particulate matter. Wave- and current-driven sediment transport across the shelves, known as wave- and current-supported turbidity currents (WCSTCs), are one of the sediment-routing processes. The studies in the last three decades suggest that WCSTCs are/were ubiquitous in modern/ancient oceans (Bhattacharya et al., 2016; Denommee et al., 2016; Fain et al., 2007; Hale & Ogston, 2015; Jaramillo et al., 2009; Ma et al., 2008, 2010; Macquaker et al., 2010; Martin et al., 2008; Ogston et al., 2008; Traykovski et al., 2000, 2007, 2015; Walsh et al., 2004; Zang et al., 2020; Zhang et al., 2016; Peng et al., 2022; Ayranci et al., 2012).

Recent studies provide evidence to that these slowly moving sediment suspensions can trigger self-driven turbidity currents toward the shelf break (Ma et al., 2008; Sequeiros et al., 2019), which swiftly transport sediments to the deep ocean. Especially, the analysis of turbidity currents over the Malaylay Canyon in the Phillippines between 2006 and 2016 (Sequeiros et al., 2019) suggests that sediments suspended in the shallow parts of the Malaylay Bay ($\sim$15 m) slowly move toward the shelf break and transition to a self-driven turbidity current. Similarly, observations on the Waipou Shelf in New Zealand showed that wave- and current-driven sediment suspension thickened towards the shelf break (Ma et al., 2008), again suggesting a trigger of a turbidity current from slowly moving WCSTCs. However, little is known as to the critical conditions that transform WC-

STCs to self-driven turbidity currents. To this end, there is a need to identify the physical processes that stabilize and destabilize WCSTCs and the parameters thereof.

The slow motion of WCSTCs across the continental shelf, thus their long sustenance in time, suggests an equilibrium. The aforementioned equilibrium is the key assumption of the existing conceptual framework for WCSTCs (Wright et al., 2001), which was rigorously analyzed and verified recently in Flores et al. (2018). The equilibrium mentioned requires a steady velocity and concentration, which thus requires a balance between downslope gravity force and the opposing shear force at the bed. Acceleration of the cross-shelf turbidity current is the natural indicator of a slow-moving WCSTC to rapid self-driven turbidity current. This acceleration is possible when downslope gravity force exceeds the friction force due potentially to sharpening shelf slope, sediment entrainment in excess of deposition, or both. Conceivably, all these conditions lead to nonlinear growth of velocity and concentration. For example, sediment entrainment in excess of deposition augments the cross-shelf gravity force and augmented cross-shelf gravity force leads to further sediment entrainment from the bed. As will be discussed in detail throughout, sediment-induced density stratification works against the described positive feedback loop as an equilibrium-restoring agent. Sediment-induced density stratification is also nonlinear because of its dissipative effect on turbulence, which thus reduces sediment suspension (see the review in Winterwerp (2001) and the references therein). Therefore, the critical conditions for the trigger of self-driven turbidity current must be based on the quantification of the competition between these two nonlinear processes, namely the positive feedback loop between sediment entrainment and the downslope gravity force as well as the sediment-induced density stratification.

Yet, as will be discussed in the following subsection, the nonlinear processes cannot be implemented into the existing models for WCSTCs. To this end, we will first summarize the available conceptual framework for WCSTCs in Section 1.2 and critically review this framework in Section 1.3 in light of the studies that followed in the literature.

Section 1.3 also summarizes the specific objectives and the hypotheses behind the objectives.

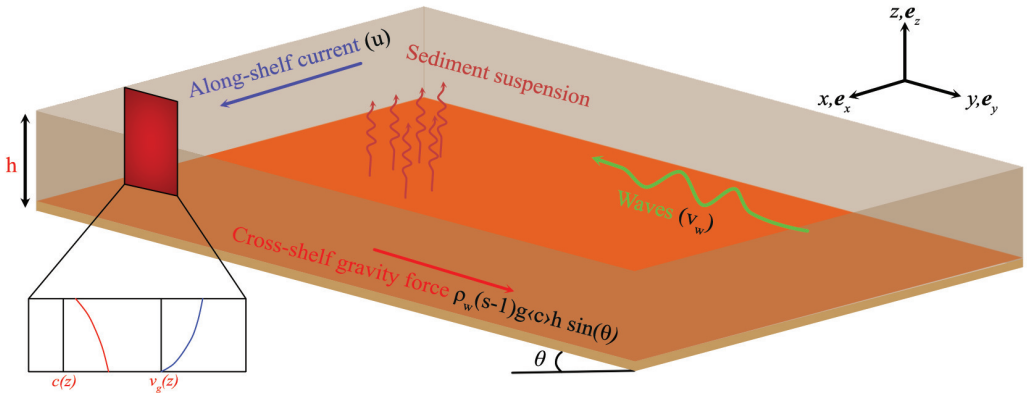

Figure 1: Descriptive sketch of WCSTCs. In the three-dimensional Cartesian coordinate system, $x-$, $y-$, and $z-$directions refer to the along-shelf, cross-shelf, and vertical directions, respectively. $\boldsymbol{e}_x$, $\boldsymbol{e}_x$, and $\boldsymbol{e}_z$ are the unit vectors in $x-$, $y-$, and $z-$directions. Along-shelf current, indicated by the blue arrow, with velocity u and shore-normal waves, indicated by undulated green arrow, with a root-mean-square wave velocity of v_w suspend sediment from the bed, which is indicated by undulated red arrows. The concentration profile of the sediment suspension is plotted in red illustrated on the panel at the bottom left corner. Sediment suspension creates a downslope gravity force of $(\rho_s - \rho_w)g\langle c\rangle h \sin\theta$, which also creates a downslope motion, whose velocity profile is shown in blue curve on the panel in the lower left corner.

1.2 Wright et al. (2001)'s Conceptual Framework

The peculiar characteristic of WCSTCs, which makes WCSTCs different from self-driven turbidity currents, is their requirement of wave and current boundary layer turbulence for their sustenance. In other words, sediments are kept in suspension with the aid of turbulence; if turbulence is removed, suspended sediments will deposit because the slow cross-shelf motion cannot sustain itself. Due to the equilibrium mentioned in Section 1.1, there is a balance between the cross-shelf gravity force and the friction force at the bed, which is formulated as

$$(s-1)g\langle c\rangle h\sin\theta = C_d v_g \sqrt{v_g^2 + v_w^2 + u^2}, \tag{1}$$

where s is the specific gravity of suspended sediments, g is the gravitational acceleration, h is the thickness of the turbidity, θ is the angle of cross-shelf bed slope, C_d is

the drag coefficient, v_g is the cross-shelf velocity of WCSTC, v_w is the wave velocity, and u is the alongshelf current velocity. Note that Equation 1 is cast by using the reference coordinate system in Figure 1. Volumetric sediment concentration is denoted as c, and the concentration used in Equation 1 is the depth-averaged concentration, where depth-averaged quantities are denoted as angled brackets. For the drag coefficient, $C_d \approx 0.003-0.006$ was proposed as a proper range of drag coefficient by referring to Komar (1977) and van Kessel & Kranenburg (1996).

Wright et al. (2001) also suggested that depth-averaged concentration is controlled by the density stratification, which is quantified by the bulk Richardson number

$$\mathrm{Ri}_b = \frac{(s-1)g\langle c\rangle h}{v_g^2 + v_w^2 + u^2}. \tag{2}$$

Bulk Richardson number was argued to be a close approximation of gradient Richardson number, where concentration gradient is approximated to $\partial c/\partial z \approx \langle c\rangle/h$, and the square of the velocity gradient is approximated to $(\partial v/\partial z)^2 \approx (v_g^2 + v_w^2 + u^2)/h^2$. It was proposed that sediment suspension in WCSTCs must be critically stratified, and the bulk Richardson number must be $\mathrm{Ri}_b = 0.25$ for critical density stratification. If stratification is weaker than critical density stratification ($\mathrm{Ri}_b < 0.25$), sediment deficit will be compensated by sediment entrainment. If stratification is stronger than the critical stratification ($\mathrm{Ri}_b > 0.25$), the excess suspension will deposit. For known v_g, v_w, and u, the suspended sediment load can be determined conveniently by imposing $\mathrm{Ri}_b = 0.25$.

By combining Equations 1 and 2, imposing $v_g \gg u_w, v$ for self-supporting turbidity current, assuming $C_d = 0.003$ as the proper drag coefficient value, and using $\mathrm{Ri}_b = 0.25$ as the critical value for density stratification, Wright et al. (2001) obtained the critical slope to maintain a self-supporting turbidity current as $\sin\theta = C_d/\mathrm{Ri}_b = 0.003/0.25 = 0.012$.

1.3 Objectives

The described conceptual framework is only applicable to steady-state conditions because equilibrium is strictly enforced. The fact that there is no term associated with the sediment concentration's time rate of change —which would quantify the growth or decay in time— disallows WCSTC's growth into self-driven turbidity current. Equilibrium is enforced by imposing density stratification as the sole governing agent of sediment entrainment and deposition. This imposition ignores the potential role of fine sediment entrainment relations, which is well-established in the literature (see Sanford & Maa (2001) for an in-depth review). Quantifying sediment entrainment through density stratification cannot capture the positive feedback loop between sediment entrainment and downslope gravity force, which potentially triggers self-driven turbidity currents. This makes it impossible to calculate the triggering conditions from the available conceptual framework. It must be noted that the critical slope of 0.012 in Wright et al. (2001) is not the critical slope that triggers turbidity current but the minimum slope to maintain a self-supported turbidity current. This is because the trigger refers to the initiation of a rapidly moving transient turbidity current; whereas the self-supporting turbidity current is the self-driven turbidity current that forms after the aforementioned transient turbidity current reaches a steady state.

The disagreement in bulk Richardson numbers reported in the literature can perhaps be explained by the role of sediment entrainment parameters on the total suspended sediment load. Recent field observations close to the Rhine River mouth (Flores et al., 2018), numerical simulations for wave-supported turbidity currents (Yue et al., 2020), wave boundary layers (Cheng et al., 2015), alongshelf current supported turbidity currents (Haddadian et al., 2021), and laboratory experiments in oscillating water tunnel (Hooshmand et al., 2015) reported Ri_b as low as 0.01. To explain the reported discrepancy in Ri_b different arguments can be made. One can ascribe this discrepancy to winnowing (Parsons et al., 2007; Flores et al., 2018). For field and laboratory studies, win-

nowing can perhaps be a plausible but unproven explanation. However, numerical experiments (Yue et al., 2020; Cheng et al., 2015; Haddadian et al., 2021) were conducted for uniform sediment size; therefore, winnowing is not a valid explanation for low Ri_b in numerical simulations.

In this study, a dynamic (time-dependent) depth-integrated concentration model is developed. The model developed accounts for sediment entrainment from and deposition to the bed as well as the density stratification. Non-linearities associated with the positive feedback loop between the sediment entrainment and the downslope gravity force as well as the density stratification are analytically approximated and incorporated into the model. This model is used to determine the trigger conditions of self-driven turbidity current that grows out of alongshelf current-supported turbidity currents (ACSTCs) and the amount of total suspended sediment load in ACSTCs. The motivation behind developing this model is to test the following hypotheses. First, *the total suspended sediment load is regulated by the equilibrium among sediment entrainment, deposition, and the density stratification created by the sediment suspension.* Second, because sediment deposition is governed mainly by settling velocity, and the sediment entrainment is governed by the erosion parameters, *both the total suspended sediment amount and the critical conditions for the self-driven turbidity current trigger are functions of settling velocity, entrainment parameters, and the parameters that quantify density stratification.* Testing these hypotheses will therefore test the validity of whether the critical density stratification is a required condition in ACSTCs.

The reason behind choosing ACSTCs in this study is twofold. First, toward the shelf break waves lose intensity or vanish because of the increasing depth, making alongshelf currents the dominant, perhaps the only, hydrodynamic driver. Second, ACSTCs have relatively simpler hydrodynamics. In the presence of waves, nonlinear interactions among waves, alongshelf currents, and cross-shelf propagation of the turbidity current will make the problem more complicated, making it hard to draw conclusions as to the

role of density stratification. For example, the augmented drag coefficient when waves and the cross-shelf propagation aligns (Yue et al., 2020) is a result of the nonlinearity mentioned. In this regard, a systematic reductive approach —starting with a simplified case that will step-by-step include further complexities— will be more appropriate to understand the respective role of each mechanism in WCSTCs.

The rest of the paper is structured as follows. In Section 2, numerical methods and the terminology will be described. Section 3 will present the overall results. In Section 4, the development of a depth-integrated suspended sediment concentration model will be described, and the validation of the model against the simulation results will be presented. Section 5 will summarize the findings with discussions.

2 Methods

2.1 Problem Setup and Governing Equations

Direct numerical simulations (DNSs) are conducted over a smooth channel with a mild spanwise slope, in which sediment entrainment is allowed at the bottom boundary. The spanwise slope creates a gravity force similar to those that drive the cross-shelf propagation of ACSTCs. Sediment velocity ($\boldsymbol{u}^s$) is obtained after the vectorial sum of the fluid (seawater) velocity ($\boldsymbol{u}^f$) and the settling velocity of sediments (w_s):

$$\boldsymbol{u}^s = \boldsymbol{u}^f + w_s \boldsymbol{e}_g, \tag{3}$$

where $\boldsymbol{e}_g$ is the unit vector in the gravitational direction with respect to the bed, that is $\boldsymbol{e}_g = (0, \sin\theta \boldsymbol{e}_y, -\cos\theta \boldsymbol{e}_z)$ with $\boldsymbol{e}_x$, $\boldsymbol{e}_y$, and $\boldsymbol{e}_z$ being the unit vectors pointing in the along-shelf, cross-shelf, and the bed-normal directions, respectively (see Figure 1). Sediment settling velocity is calculated as

$$w_s = \frac{(s-1)gd^2}{18\nu^f}, \tag{4}$$

following the Stokes law, which is valid for fine spherical sediments. In Equation 4, d is the sediment diameter and ν^f is the kinematic viscosity of the seawater. The diameter range of sediments used in he simulations ($d = [6 \times 10^{-6}, 20 \times 10^{-6}]$ m) is sufficiently small to use the Stokes Law for the sediment settling velocity.

As it will be shown in Section 3.2, sediment concentration does not exceed 2 kg m^{-3}, suggesting that sediment suspension is dilute. Dilute sediment suspension allows us to impose the continuity equation for the seawater:

$$\boldsymbol{\nabla} \cdot \boldsymbol{u}^f = 0. \tag{5}$$

The momentum equation of the seawater is given as

$$\frac{\partial \boldsymbol{u}^f}{\partial t} + \boldsymbol{u}^f \cdot \boldsymbol{\nabla}\boldsymbol{u}^f = \frac{u_{\tau o}^2}{h}\boldsymbol{e}_x + \frac{1}{\rho}\boldsymbol{\nabla}p' + (s-1)gc\,\boldsymbol{e}_g + \nu^f \boldsymbol{\nabla}^2 \boldsymbol{u}^f. \tag{6}$$

Here, the friction velocity due to alongshelf current is denoted as $u_{\tau o} = \sqrt{\tau_{bo}/\rho^f}$, where τ_{bo} and ρ^f are the bed shear stress due to alongshelf current and the density of the seawater, respectively. The alongshelf current is driven by a uniform pressure gradient equal to $u_{\tau o}^2/h$, where h is the flow depth and is the first term on the right-hand side of Equation 6. When integrated along the bed-normal direction, this term will counter the bed shear stress created by the along-shelf current normalized by the density of the seawater per unit mass, that is τ_{bo}/ρ^f. The second term on the right-hand side will both force the cross-shelf flow through $(s-1)gc\,\sin\theta\boldsymbol{e}_y$ and accounts for the density stratification due to vertical buoyancy force $-(s-1)gc\,\cos\theta\boldsymbol{e}_z$.

The governing equation for the suspended sediment concentration is the advection-diffusion equation, valid for fine sediment suspension (Cantero et al., 2008). The advection-diffusion equation is given as

$$\frac{\partial c}{\partial t} + \boldsymbol{u}^s \cdot \boldsymbol{\nabla} c = \mathcal{D} \boldsymbol{\nabla}^{\mathbf{2}} c, \tag{7}$$

where $\mathcal{D}$ is the effective diffusivity of the sediment concentration, which is selected to be equal to the kinematic viscosity of the seawater.

2.2 Computational Domain and Boundary Conditions

The governing equations are solved for a planar computational domain. The size of the domain in $x-$, $y-$, and $z-$directions is $4\pi h \times 2\pi h \times h$. The number of grid points in the corresponding directions is $256 \times 128 \times 257$. The selected domain size is sufficient to capture the largest eddies, and the resolution is sufficient to resolve the smallest eddy size formed. A detailed discussion regarding the domain size selection will follow in Section 2.3.

Periodic boundary conditions in $x-$ and $y-$directions are specified for concentration and velocity. Given that the equilibrium conditions are established in ACSTCs, choosing periodic boundary conditions in $x-$ and $y-$directions is proper. At the bed, a no-slip boundary condition is imposed for the fluid velocity. The top boundary for the fluid phase is defined as a rigid lid, wherein the fluid can slip in $x-$ and $y-$directions, but the vertical motion is not allowed, that is $\partial u^f / \partial z = \partial v^f / \partial z = 0$, and $w^f = 0$ at $z = h$.

The bottom boundary condition for sediment entrainment is specified following the previous studies (Cheng et al., 2015; Yue et al., 2020; Haddadian et al., 2021):

$$-\mathcal{D} \frac{\partial c}{\partial z} - w_s \, c \Big|_{z=0} = \mathscr{E} - \mathscr{D}, \tag{8}$$

where $\mathscr{E}$ and $\mathscr{D}$ respectively refer to the erosion and deposition fluxes. For the erosion flux, Partheniades-Arthurai-type formulation is adopted (Sanford & Maa, 2001)

$$\mathscr{E} = \begin{cases} m_e \left(\frac{||\tau_b \cdot \boldsymbol{s}||}{\tau_c} - 1 \right), & \text{if } ||\tau_b|| > \tau_c \\ 0, & \text{if } ||\tau_b|| < \tau_c \end{cases}, \tag{9}$$

where m_e is the erosion rate, and τ_c is the critical shear stress for erosion. $||\tau_b \cdot \boldsymbol{s}||$ is the magnitude of the tractive (or shear) force over a unit area with $\boldsymbol{s}$ being the unit vector pointing in the shear force direction at the bed. Magnitude-wise, bed shear stress and the shear force over a unit area are the same. Because shear stress is a tensor, it has to be vectorized to account for the along- and cross-shelf shear force components, leading to the notation in Equation 9 and the equations that follow. The deposition flux is calculated as

$$\mathscr{D} = w_s \, c \Big|_{z=0}. \tag{10}$$

2.3 Parameter Selection

As it will be clearer in Section 3, the analytical model developed for the depth-integrated concentration is significantly affected by the sediment-induced density stratification. Therefore, the scales associated with turbulence and density stratification must be resolved. Resolving the scales mentioned arguably requires using DNS. On the other hand, simulating ACSTCs at a realistic scale by DNS is almost impossible due to computational requirements. To this end, a downscaled ACSTC, which will be referred to as miniature ACSTC (Haddadian et al., 2021), will be used. For the miniature ACSTC, the flow depth is selected as $h = 0.10$ m, the initial bed shear stress is $\tau_{bo} = 0.013$ Pa, the critical shear stress is selected as $\tau_c = 0.01$ Pa. The bed shear stress imposed corresponds to a friction velocity of $u_{\tau o} = 0.0036$ m s^{-1}. The importance of friction velocity arises because it scales the velocity profile, which affects the Reynolds number. For developed turbulence to occur, the Reynolds number must be sufficiently high so that scale change will minimally impact the turbulent features. With the imposed friction velocity, one can

obtain the Reynolds number as $Re = 7 \times 10^4$ (see Haddadian et al., 2021), where the Reynolds number is defined as

$$Re = \frac{\langle u \rangle h}{\nu^f}. \tag{11}$$

In Equation 11, $\langle u \rangle$ is the depth-averaged along-shelf velocity.

Downscaling ACSTCs will especially require the idealization of the critical shear stress and the scales associated with sediment transport. Although the turbulent flow is developed, the bed shear stress, which is $\tau_{bo} = 0.013$ Pa, can only erode loose fine sediments at the bed (Curran et al., 2007). Increasing the bed shear stress, even slightly, will add significant computational expense due to the increasing Reynolds number. Therefore, we selected the critical bed shear stress as $\tau_c = 0.010$ Pa and the entrainment rate $m_e = 3.6 \times 10^{-7}$ m s^{-1}, which are close to what has been used in previous studies for wave boundary layers (Cheng et al., 2015; Yue et al., 2020) and ACSTCs (Haddadian et al., 2021).

As it will be described in Section 3.2, settling velocity is the key parameter to change the density stratification and the sediment mass exchange at the bed. Therefore, sediment settling velocity normalized by the friction velocity is varied from $w_s/u_{\tau o} = 0.01$ to $w_s/u_{\tau o} = 0.1$ (see Table 1 for $w_s/u_{\tau o}$ values used in each simulation). Because the nonlinearity associated with the sediment entrainment and the cross-shelf gravity force in part depends on the cross-shelf bed slope, that is $\sin\theta$, specifying two different values for $\sin\theta$ will provide us with a wide range of cross-shelf gravity force to assess the nonlinearity mentioned.

Table 1: Simulated cases and input parameters.

Case	$w_s/u_{\tau o}$	$\sin\theta$	$m_e/u_{\tau o}$	τ_{bo}/τ_c
A1	0.10	0.01	1×10^{-4}	0.25
A2	0.08	0.01	1×10^{-4}	0.25
A3	0.06	0.01	1×10^{-4}	0.25
A4	0.04	0.01	1×10^{-4}	0.25
A5	0.02	0.01	1×10^{-4}	0.25
A6	0.01	0.01	1×10^{-4}	0.25
B1	0.10	0.005	1×10^{-4}	0.25
B2	0.08	0.005	1×10^{-4}	0.25
B3	0.06	0.005	1×10^{-4}	0.25
B4	0.04	0.005	1×10^{-4}	0.25

Although idealized, the simulations will guide the development of the depth-integrated concentration model and validate the model results. Especially, sediment turbulence interaction, significantly altering the suspended sediment load, is resolved through DNS. The fidelity of the simulations to capture the fluid-sediment interaction will be presented in Section 3.2.

2.4 Numerical Methods

The governing equations are integrated in time by a third-order low-storage Runge-Kutta scheme (Williamson, 1980) with a maximum Courant-Friedrichs-Lewy number of 0.5. Applying the pseudospectral scheme following Cortese & Balachandar (1995), the carrier flow phase is numerically solved with the corresponding boundary conditions (Equation 8). During each of the three time levels in a computational step, the standard two-stage (predictor and corrector) projection method (Chorin, 1968) is utilized to enforce a divergence-free velocity field of the carrier flow. Right after the velocity projection, that is Equation 7, the sediment volumetric concentration is computed by solving the advection-diffusion equation in a way similar to the predictor stage of carrier flow with the corresponding boundary conditions. For further details, the reader is referred to Yue et al. (2019).

2.5 Notation and Terminology

Because different averaging techniques will be used, defining the averaging techniques in this subsection will provide convenience to the reader. Mean velocity and concentration, discerned by an overbar, are obtained after averaging them over each horizontal plane at every vertical point and the sampling time T:

$$\bar{(\cdot)} = \frac{1}{L_x\, L_y\, T} \int_{t_o}^{t_o+T} \int_{y=0}^{y=L_y} \int_{x=0}^{x=L_x} (\cdot)\, \mathrm{d}x\, \mathrm{d}y\, \mathrm{d}t, \tag{12}$$

where t_o is the initial time of equilibrium. Note that mean quantities vary in depth. Whether the flow reached equilibrium was identified as the instant when the time series of the depth-averaged quantities', such as velocity and Reynolds shear stress, moving average becomes constant. The moving average is calculated over a period of 5.44 seconds. For reliable turbulence statistics, T is ensured to be long enough so that the averaged quantities become insensitive to increasing T. Depth-averaged quantities, indicated by angled brackets, are computed from

$$\langle \cdot \rangle = \frac{1}{h} \int_{z=0}^{z=h} \bar{(\cdot)}\, \mathrm{d}z. \tag{13}$$

3 Results and Discussions

3.1 Overview

The conducted simulations resulted in two unstable cases wherein the depth-averaged sediment concentration grew substantially, which is presented in Figure 2. The two cases mentioned correspond to the lowest settling velocity, namely $w_s/u_{\tau o} = 0.01$ and 0.02 for $\sin\theta = 0.01$. In these two cases, there is no sign of equilibrium, but instead, the concentration started accelerating past a certain time step, which is 360 s and $t = 840$ s for $w_s/u_{\tau o} = 0.01$ and 0.02, respectively. It is concluded that a self-driven turbidity current formed, and the simulations were terminated shortly after those instants. The rea-

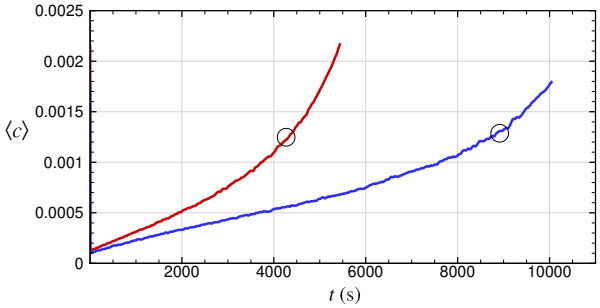

Figure 2: Time series of depth-averaged volumetric sediment concentration of the two unstable cases with $w_s/u_{\tau o} = 0.01$ and $w_s/u_{\tau o} = 0.02$ in which the cross-shelf slope is $\sin\theta = 0.01$. In both cases, suspended sediment concentration substantially grows without showing a sign of equilibrium, and the growth rate increases past a critical instance marked by a hollow circle, which is inferred from the time series of $\partial\langle c\rangle/\partial t$ (not shown).

son for termination is that the small domain size can only capture the very early stage of self-driven turbidity current growth. As sediments get finer, they can be easily suspended to elevations higher than the domain height. In the current setup, however, they are entrapped in a small domain due to no sediment outflux at the top. As such, sediment concentration will grow in a bounded domain, a physical situation irrelevant to the growth of self-driven turbidity currents after its very early stage. In this regard, the small domain for the miniature representation of ACSTCs is not sufficient to capture the whole process of self-driven turbidity current growth but its early stages. Indeed, these two simulations fall into the unstable region in the parametric space, that is, the region of ACSTCs' transition to self-driven turbidity currents, which will be discussed in detail in Section 4.3.1.

For stable cases, the time series of the bulk Richardson number is plotted in Figure 3a instead of depth-averaged concentration. Doing so will serve to assess whether the bulk Richardson number reaches a global constant value, which was suggested in the previous studies (Wright et al., 2001; Wright & Friedrichs, 2006). Because conclusions from the Ri_b time series are similar for both slopes, Figure 3a plots Ri_b time series for only $\sin\theta = 0.01$ for brevity. Figure 3a suggests that Ri_b equilibrates at different values for different sediment settling velocities, and its order of magnitude is almost a decade

smaller than 0.25. Another observation is that the bulk Richardson number gets larger with decreasing settling velocity. From the definition of Ri_b, one may conjecture that velocity and the density gradients may not be accurately captured in Ri_b to measure the density stratification. In Figure 3b, we, therefore, plot the gradient Richardson number profiles, which is a stronger measure of density stratification. The gradient Richardson number, Ri_g, is defined as

$$\mathrm{Ri}_g = -\frac{(s-1)g\frac{\partial \overline{c}}{\partial z}}{\left(\frac{\partial \overline{u}_g}{\partial z}\right)^2 + \left(\frac{\partial \overline{v}}{\partial z}\right)^2}. \tag{14}$$

Profiles of Ri_g from the simulations do not collapse onto a single curve. Especially outside the near-bed region, the values of Ri_g decrease with increasing settling velocity. The magnitude range of Ri_g is almost three times that of Ri_b, especially outside the near-bed region. Our first conclusion from the time series of Ri_b and profiles of Ri_g is that the bulk Richardson number does not adequately capture the sediment-induced density stratification because there is a significant mismatch between the magnitudes of Ri_g and Ri_b. Because the gradient Richardson number profiles differ in magnitude despite the equilibrium, our second conclusion is that critical density stratification does not occur in the current simulations. This strengthens our hypothesis on the regulatory role of sediment entrainment and deposition on the total suspended sediment load. In the following subsection, eddy diffusivity and suspended sediment concentration profiles will be presented and analyzed regarding the respective roles of density stratification and the sediment mass exchange at the bed.

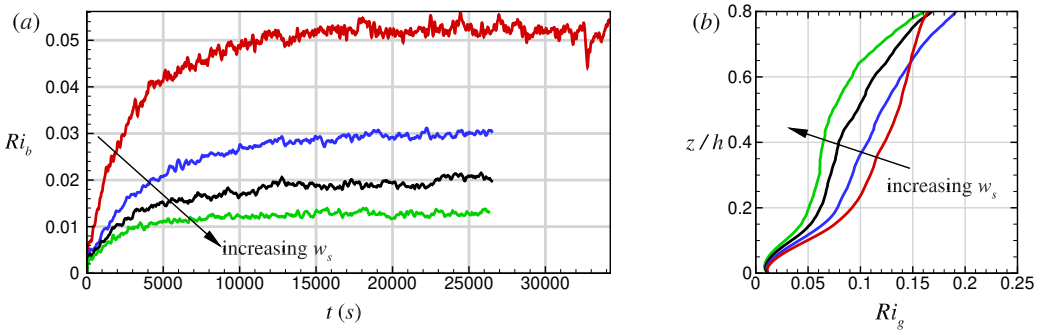

Figure 3: (a) Time series of bulk Richardson number for cases with $\sin\theta = 0.01$. The arrow indicates the reduction of Ri_b in magnitude with increasing w_s. Time series of Ri_b for $\sin\theta = 0.005$ also shows a similar trend and is therefore not shown for brevity. (b) Gradient Richardson number profiles for the same cases in panel (a). In both subfigures, red, blue, black, and green curves indicate $w_s/u_{\tau o}$=0.04, 0.06, 0.08, and 0.10, respectively.

3.2 Concentration and Eddy Diffusivity Profiles

To facilitate an informed discussion on the role of sediment entrainment, deposition, and density stratification on the amount of suspended sediment concentration, let us momentarily ignore the effects of density stratification. In the absence of density stratification, the amount of sediment suspension depends on the sediment entrainment at the bed and the shape of the concentration profile, which are tightly linked to the settling velocity, w_s. The shape of the concentration profile is important because the rate of deposition will increase as the concentration profile is skewed towards the bed. The role of w_s on the shape of the concentration profile can be realized through the balance between the settling flux, $w_s\bar{c}(z)$, and the turbulent suspension $\overline{c'w'}$, which can also be quantified as $-\mathcal{D}_t\, d\bar{c}/dz$:

$$-\mathcal{D}_t \frac{d\bar{c}}{dz} = w_s \bar{c}(z). \tag{15}$$

The concentration gradient, which can be considered as a proxy for the shape of the concentration profile, becomes $-w_s\bar{c}/\mathcal{D}_t$. This suggests that decreasing w_s or increasing $\mathcal{D}_t$ makes the concentration profile's shape more uniform; whereas increasing w_s or decreasing $\mathcal{D}_t$ skews the sediment concentration towards the bed. It is clear that sed-

iment settling velocity is one of the governing parameters of the concentration profile's shape, even in the absence of density stratification. Sediment settling velocity is also a governing parameter of sediment mass exchange at the bed, which can be realized after rearranging the bottom boundary condition for sediment concentration at the bed, that is, $c_b = m_e/w_s(\overline{\tau}_b/\tau_c - 1)$.

It is worth noting that Equation 15 also provides us with the required resolution to quantify the density, or concentration, gradient, which is $\mathcal{D}_t/w_s$. The eddy diffusivity varies with depth and approaches zero towards the bed. As such, there is a high resolution requirement, especially near the bed, which cannot be captured by the bulk Richardson number.

When density stratification is present, the role of settling velocity on the shape of the concentration profile becomes convoluted. This is because settling velocity is also a governing parameter of sediment-induced density stratification and the turbulence dissipation thereof (Winterwerp, 2001; Cantero et al., 2012; Winterwerp et al., 2009; Ozdemir et al., 2011; Haddadian et al., 2021). With turbulence is dissipated, sediment mixing reduces, and so does the eddy diffusivity. The shape of the concentration profile, therefore, changes in concert with the shape of the eddy diffusivity profile. In this regard, throughout this section, simulated concentration profiles are mostly presented in the context of their shape, the balance between deposition and sediment entrainment, and the governing parameters thereof.

For informed interpretation, it is worth discussing the application of the Monin-Obukhov theory in stratified sediment-laden flows, on which we will construct our model. The eddy diffusivity and suspended sediment concentration profiles in stratified sediment-laden flows can be obtained by using the Monin-Obukhov theory (Monin & Obukhov, 1954). From the Monin-Obukhov theory, the eddy diffusivity profile is obtained as

$$\mathcal{D}_t = \frac{u_{\tau o}\kappa z}{S_c}\left(\frac{1-\frac{z}{h}}{1+\alpha\frac{z}{\mathcal{L}}}\right), \tag{16}$$

where $\mathcal{L}$ is the Monin-Obukhov length scale, and κ is the von Kármán constant. The Schmidt number, S_c, is the ratio between the eddy viscosity (ν_t) and the sediment diffusivity ($\mathcal{D}_t$), that is $S_c = \nu_t/\mathcal{D}_t$. α is an empirical coefficient, which was proposed to be 5 in (Monin & Obukhov, 1954). It is worth noting that the Monin-Obukhov length scale ($\mathcal{L}$) measures the turbulence production relative to the buoyancy dissipation. As such, increasing $\mathcal{L}^{-1}$ suggests strengthening buoyancy dissipation relative to turbulence production (see Winterwerp et al., 2009; Haddadian et al., 2021, for further discussion). As was shown in Winterwerp et al. (2009) and Haddadian et al. (2021) the ratio between the depth (h) and the Monin-Obukhov length scale ($\mathcal{L}$), which will be denoted as the Monin-Obukhov parameter ($\mathcal{M}$) henceforth, can be expressed in terms of the settling velocity (w_s), friction velocity ($u_{\tau o}$), and the depth-averaged concentration ($\langle c\rangle$):

$$\mathcal{M} = \alpha\frac{h}{\mathcal{L}} = \alpha\frac{(s-1)g\langle c\rangle h}{u_{\tau o}^2}\frac{w_s}{u_{\tau o}}. \tag{17}$$

By using the Monin-Obukhov parameter, eddy diffusivity profile can also be expressed as

$$\mathcal{D}_t = \frac{u_{\tau o}\kappa z}{S_c}\left(\frac{1-\frac{z}{h}}{1+\mathcal{M}\frac{z}{h}}\right). \tag{18}$$

From Equation 17 and Equation 18, it is clear that both increasing concentration and settling velocity dissipate eddy diffusivity and are the governing parameters of density stratification. Eddy diffusivity profile in Equation 18 allows for an analytical solution of the sediment concentration profile (Itakura & Kishi, 1980):

$$c = c_o \left(\frac{z}{z_o} \frac{h - z_o}{h - z} \right)^{-\mathcal{R}} \left(\frac{h - z_o}{h - z} \right)^{-\mathcal{R}\mathcal{M}}. \tag{19}$$

where z_o is the reference height, c_o is the reference concentration, and $\mathcal{R} = w_s/(S_c \kappa u_{\tau o})$ is the Rouse number. Note that the definition of the Rouse number here includes the Schmidt number (S_c) to make the following equations concise. Without the last term on the right-hand side, the concentration profile becomes identical to the Rouse profile, which is

$$c = c_o \left(\frac{z}{z_o} \frac{h - z_o}{h - z} \right)^{-\mathcal{R}}. \tag{20}$$

The concentration profile in Equation 19 will therefore be referred to as the modified Rouse profile henceforth.

The eddy diffusivity and concentration profiles obtained from the simulations are presented in Figure 4. In Figure 4a, the close match between the observed eddy diffusivity profiles from the simulations and those estimated by Equation 16 is obtained by treating α, the empirical coefficient in Monin-Obukhov's self-similarity function, as a free variable. α ranges between $\alpha = 3.8$ and $\alpha = 4.7$ (see Table 1), which is similar to those reported in Haddadian et al. (2021). It is worth mentioning that α approaches 5 with strengthening density stratification. This point deserves further investigation but not within the scope of this study. The Schmidt number S_c used to obtain the eddy diffusivity profiles are the depth-averaged values of S_c between $z/h = 0.1$ and $z/h = 0.9$ because turbulence becomes prevalent in the range selected (see Figure 4b for the profiles of S_c). The range of Schmidt number is $S_c = [0.89, 1]$, which falls onto its suggested values (Cellino & Graf, 1999). Eddy diffusivity profiles are also compared with their parabolic counterpart that develops in non-stratified media (dashed black curve in Figure 4a). This comparison suggests a reduction in the magnitude of the eddy diffusivity with decreasing settling velocity, which clearly indicates enhanced turbulence dissipation with decreasing settling velocity. This is mainly because sediment suspension increases with the reduc-

Table 2: Observed parameters from the simulations that reached equilibrium. Cases A5 and A6, which are excluded from the table, are the unstable cases; therefore, a quasi-steady depth-averaged concentration and velocity cannot be obtained.

Case	S_c	α	$\langle c \rangle \times 10^5$	$\mathcal{M}$	$\langle v_g \rangle$ (m s^{-1})	$\langle u \rangle$ (m s^{-1})	$\langle u_{max} \rangle$ (m s^{-1})	Ri_b
A1	0.89	4.00	4.04	2.02	2.9×10^{-3}	71.40×10^{-3}	71.50×10^{-3}	0.013
A2	0.90	4.10	6.83	2.80	5.4×10^{-3}	74.80×10^{-3}	75.00×10^{-3}	0.020
A3	1.00	4.10	12.40	3.81	10.3×10^{-3}	80.40×10^{-3}	81.00×10^{-3}	0.031
A4	1.00	4.40	29.14	6.41	27.4×10^{-3}	91.10×10^{-3}	95.10×10^{-3}	0.052
B1	0.89	0.89	4.04	1.97	1.4×10^{-3}	71.30×10^{-3}	71.30×10^{-3}	0.013
B2	0.92	0.92	6.67	2.53	2.8×10^{-3}	75.00×10^{-3}	75.00×10^{-3}	0.019
B3	1.00	1.00	12.31	3.69	5.2×10^{-3}	80.10×10^{-3}.	80.20×10^{-3}	0.031
B4	1.00	1.00	25.68	5.90	12.0×10^{-3}	89.30×10^{-3}	90.10×10^{-3}	0.051

tion in the settling velocity, which will be discussed shortly in this section. The peak of the eddy diffusivity is lowered in height as density stratification intensifies.

The comparison of the modified Rouse profile with those obtained from the simulations in Figure 4(b,c) suggests a good agreement, which serves as a validation for the numerical model's fidelity to resolve turbulence and density stratification. It is worth noting that the concentration profiles in Figure 4b are normalized by the bed concentration to assess its shape. The modified Rouse profiles were obtained by choosing the reference height as $z_o = 0.01$ m, above which turbulence becomes prevalent. The modified Rouse profiles bend towards zero in the upper half of the depth when compared with the Rouse profile (compare the dashed curve with the solid curves in Figure 4c), which is consistent with the reduction in the eddy diffusivity. Reduction in concentration in modified Rouse profiles suggests a decline in total suspended sediment load with density stratification. Referring to the definition of the Monin-Obukhov parameter ($\mathcal{M}$) in Equation 17, one can conclude that the shape of the concentration profile is affected by both the settling velocity and the amount of sediment suspension.

Another observation from Figure 4c is that near-bed sediment concentration increases with decreasing w_s. This observation is closely related to the role of w_s on sed-

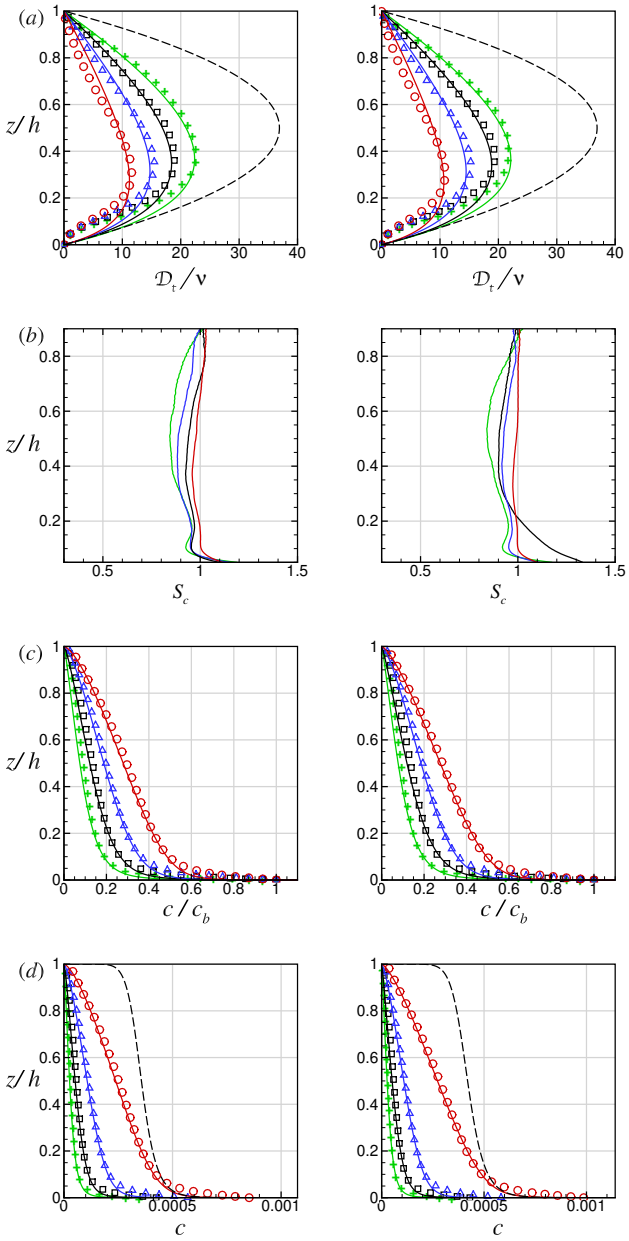

Figure 4: : (a) Eddy diffusivity profiles normalized by the kinematic viscosity. (b) Schmidt number profiles. (c) Suspended sediment concentration profiles normalized by the concentration at the bed. (d) Volumetric suspended sediment concentration profiles. The first and the second rows plots the profiles of cases with $\sin\theta = 0.005$ and $\sin\theta = 0.01$, respectively. In all subfigures, red, blue, black, and green respectively identifies $w_s/u_{\tau o} = 0.04, 0.06, 0.08$, and 0.10. Solid curves on the left column indicate the eddy diffusivity estimated by the Monin-Obukhov theory (Equation 16), and the symbols of the same color as the curves indicate those obtained from the simulations. Solid curves on the second and the third columns estimate the modified Rouse profile from Equation 20, and symbols of the same color correspond to those obtained from the simulations. The dashed curves in (a) indicate the parabolic eddy diffusivity profile that occurs in unstratified media, and the dashed curves in (c) indicate the Rouse profile for $w_s/u_{\tau o} = 0.04$ to emphasize the reduction in sediment concentration due to density stratification.

iment mass exchange at the bed. Noting that the critical shear stress for erosion is the same in all the simulations, near-bed concentration is inversely proportional to w_s, that is $\overline{c}_b \propto m_e/w_s(\overline{\tau}_b/\tau_c - 1)$.

The results presented in this section suggest that the total suspended load is governed by sediment mass exchange at the bed and density stratification. The respective contributions of each mechanism to the total suspended load will be addressed by the dynamic depth-integrated concentration model, which will be discussed in the section that follows.

4 Dynamic Depth-integrated Concentration Model

To obtain the critical conditions for self-supported turbidity current trigger, a dynamic (time-dependent) depth-integrated sediment concentration model is developed. Because equilibrium requires a statistically steady depth-integrated concentration, an equation that quantifies the depth-integrated concentration's variation in time will be a convenient tool to assess equilibrium. Upon integrating the advection-diffusion equation for the sediment concentration and neglecting the diffusive term due to its negligible magnitude as opposed to the advective terms, we obtain the following equation

$$\frac{\mathrm{d}\langle c\rangle h}{\mathrm{d}t} = \frac{\partial\langle c\rangle h}{\partial t} + u^s\frac{\partial\langle c\rangle h}{\partial x} + v^s\frac{\partial\langle c\rangle h}{\partial y} = m_e\left(\frac{||\tau_b\cdot\boldsymbol{s}||}{\tau_c} - 1\right) - w_s c_o. \tag{21}$$

The left-hand side of Equation 21 is the total derivative of the depth-integrated concentration, that is $\langle c\rangle h$. The first and the second terms on the right-hand side respectively represent the sediment entrainment and settling fluxes at the bed, which are the source and sink terms, respectively. $||\tau_b\cdot\boldsymbol{s}||$ is the magnitude of the shear force at the bed over a unit area, which is the vector sum of those created in along- and cross-shelf directions. It must be noted that Equation 21 is dimensional, and all additive terms has a unit of m s^{-1}. Yet, keeping Equation 21 dimensional will make the equations that follow lengthy, creating inconvenience to the reader. Therefore, Equation 21 is nondimen-

sionalized by normalizing each term by $u_{\tau o}$, and expressing $w_s/u_{\tau o}$ as $\kappa S_c \mathcal{R}$. In its non-dimensional form, Equation 21 reads

$$\frac{1}{u_{\tau o}} \frac{\mathrm{d}\langle c \rangle h}{\mathrm{d}t} = \frac{m_e}{u_{\tau o}} \left(\frac{||\tau_b \cdot \boldsymbol{s}||}{\tau_c} - 1 \right) - (\kappa S_c \mathcal{R}) c_o. \tag{22}$$

The dynamic depth-integrated concentration model will enable us to determine whether ACSTCs can remain in equilibrium or will grow to a self-driven turbidity current. For equilibrium, the right-hand side of Equation 22 must be zero. In other words, if erosion is countered by deposition, depth-integrated concentration will be in equilibrium; if not, there will be a growth in sediment suspension amount. The roles of density stratification and the positive feedback loop between the sediment suspension and sediment entrainment are implicit in the erosion and deposition flux terms, respectively. As it will be shown in the following two subsections, these two mechanisms nonlinearly augment or reduce the suspended sediment amount. The following two subsections describe how nonlinearity in entrainment and deposition fluxes are obtained as explicit functions of $\langle c \rangle$.

4.1 Nonlinear Effect of Alongshelf Turbidity Currents on Entrainment

In the problem specified, the critical bed shear stress for erosion and bed shear stress due to along-shelf current are assumed to be known a priori. The augmented bed shear stress due to sediment suspension can simply be inferred from the bed shear stress, which is

$$||\tau_b \cdot \boldsymbol{s}|| = \sqrt{\tau_{bo}^2 + \left[(s-1) g \langle c \rangle h \sin\theta\right]^2} \tag{23}$$

which is a function of the depth-averaged sediment concentration. To have a convenient mathematical handle on the bed shear stress magnitude, we first rearrange Equation 23 by normalizing it by τ_{bo}:

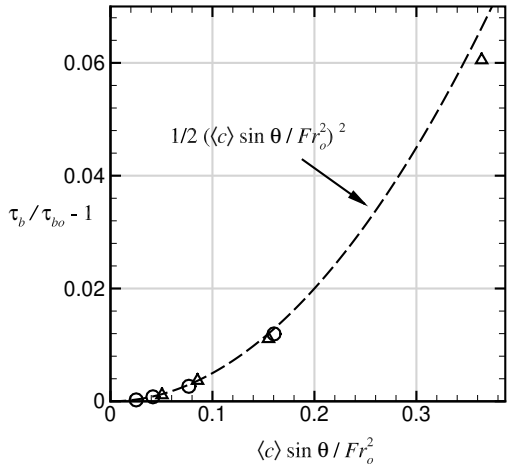

Figure 5: Variation of bed shear increase against the non-dimensional across-shelf gravity force $\frac{\langle c \rangle}{Fr_o^2} \sin\theta$. The data shown is obtained from the simulations wherein hollow circles indicate the simulated results for $\sin\theta = 0.005$, and the hollow triangles indicate those for $\sin\theta = 0.01$.

$$\frac{||\tau_b \cdot \boldsymbol{s}||}{\tau_{bo}} = \sqrt{1 + \frac{[(s-1)g\langle c \rangle h \sin\theta]^2}{\tau_{bo}^2}}. \tag{24}$$

Equation 24 can further be simplified by defining a densimetric Froude number Fr_o

$$Fr_o = \frac{u_{\tau o}}{\sqrt{(s-1)gh}}, \tag{25}$$

which will help express Equation 24 as

$$\frac{||\tau_b \cdot \boldsymbol{s}||}{\tau_{bo}} = \sqrt{1 + \left(\frac{\langle c \rangle \sin\theta}{Fr_o^2}\right)^2}. \tag{26}$$

As will be evident later in this section, expressing Equation 26 as a serial sum will help quantify the excess entrainment due to alongshelf current. The right-hand side of Equation 26 is therefore expanded as a binomial series sum:

$$\frac{||\tau_b \cdot \boldsymbol{s}||}{\tau_{bo}} = 1 + \frac{1}{2}\left(\frac{\langle c\rangle \sin\theta}{Fr_o^2}\right)^2 - \frac{1}{8}\left(\frac{\langle c\rangle \sin\theta}{Fr_o^2}\right)^4 + \frac{1}{16}\left(\frac{\langle c\rangle \sin\theta}{Fr_o^2}\right)^6 - \dots . \tag{27}$$

519 Under equilibrium conditions or at the early stages of transition to self-driven tur-
520 bidity currents, a weak nonlinearity is expected because of the dilute sediment concen-
521 tration. The serial sum can hence be approximated to its first order:

$$\frac{||\tau_b \cdot \boldsymbol{s}||}{\tau_{bo}} \approx 1 + \frac{1}{2}\left(\frac{\langle c\rangle \sin\theta}{Fr_o^2}\right)^2 . \tag{28}$$

522 Subtracting τ_{bo} from $||\tau_b \cdot \boldsymbol{s}||$ will isolate the bed shear stress increase, which is de-
523 noted as $\Delta\tau_b$, as a function of the depth-integrated sediment concentration and is given
524 as

$$\frac{||\tau_b \cdot \boldsymbol{s}|| - \tau_{bo}}{\tau_{bo}} = \frac{\Delta\tau_b}{\tau_{bo}} = \frac{1}{2}\left(\frac{\langle c\rangle \sin\theta}{Fr_o^2}\right)^2 . \tag{29}$$

525 This relation is compared with those obtained from the simulations in Figure 5.
526 The estimated and observed values of $\Delta\tau_b$ agree well with a coefficient of determination
527 of $r^2 = 0.996$, confirming the dilute suspended sediment assumption. The increase in
528 the bed shear stress due to cross-shelf propagation of ACSTCs can therefore be isolated
529 as

$$\frac{m_e}{u_{\tau o}}\left(\frac{||\tau_b \cdot \boldsymbol{s}||}{\tau_c} - 1\right) = \frac{m_e}{u_{\tau o}}\left[\left(\frac{\tau_{bo}}{\tau_c} - 1\right) + \frac{\Delta\tau_b}{\tau_c}\right]. \tag{30}$$

530 Denoting the normalized excess shear stress due to alongshelf current $\tau_{bo}/\tau_c - 1$
531 as ξ and noting that $\Delta\tau_b/\tau_c = (\Delta\tau_b/\tau_{bo})(\tau_{bo}/\tau_c)$, Equation 30 can be expressed as an
532 explicit function of $\langle c\rangle$ as follows:

$$\frac{m_e}{u_{\tau o}}\left(\frac{||\tau_b \cdot \boldsymbol{s}||}{\tau_c} - 1\right) = \frac{m_e}{u_{\tau o}}\left[\xi + \left(\frac{1+\xi}{2}\right)\left(\frac{\sin\theta}{Fr_o^2}\right)^2 \langle c\rangle^2\right]. \tag{31}$$

Nonlinearity in sediment entrainment due to cross-shelf gravity force, which is the rightmost term within the brackets, is a quadratic function of the depth-averaged suspended sediment concentration. This term represents the positive feedback loop between the suspended sediment load and the bed shear stress magnitude. The nonlinearity mentioned will be the main driver of the sediment suspension growth that will lead to self-driven turbidity currents.

4.2 Nonlinear Density Stratification Effect on Suspended Sediment Load

In Equation 22, the deposition flux is not an explicit function of $\langle c\rangle$ but expressed in terms of the bed concentration c_o. Therefore, we define a shape factor $\mathcal{S}$ that links bed concentration to depth-averaged concentration:

$$\mathcal{S} = \frac{c_o}{\langle c\rangle}. \tag{32}$$

We term $\mathcal{S}$ as the shape factor because it provides information as to the shape of the suspended sediment concentration profile (a similar definition for the shape factor is also given in Parker et al. (1986) for self-supporting turbidity currents). For example, $\mathcal{S}$ becomes unity for uniform sediment concentration, whereas $\mathcal{S}$ enlarges when concentration becomes skewed towards the bed. Strengthening density stratification will dampen eddy diffusivity, modulate the shape of the eddy diffusivity profile, and hence skew the concentration profile towards the bed. It follows that the shape factor must increase with strengthening stratification. In Section 3.2, density stratification is quantified by $\mathcal{M}$, and $\mathcal{M}$ is a function of depth-averaged concentration and settling velocity (see Equation 17). Therefore, the shape factor must be a function of both $\langle c\rangle$ and w_s. In the limit of vanishing density stratification, the shape factor $\mathcal{S}$ must approach the shape factor of the

554 Rouse profile, $\mathcal{S}_{\mathcal{R}}$, which is independent of $\langle c \rangle$, or $\mathcal{M}$. As stratification strengthens, the
555 shape factor must reflect the effect of density stratification. To this end, we impose the
556 following functional form for $\mathcal{S}$:

$$\mathcal{S}(\mathcal{R}, \mathcal{M}) = \mathcal{S}_{\mathcal{R}}(\mathcal{R})\, f(\mathcal{R}, \mathcal{M}), \tag{33}$$

557 where f quantifies the amplification of $\mathcal{S}$ due to density stratification. In the limit
558 of vanishing density stratification, f must approach unity to ensure the concentration
559 profile is Rousean. When density stratification strengthens, f must increase. The given
560 mathematical form in Equation 33 requires the quantification of $\mathcal{S}_{\mathcal{R}}$ and f. To deter-
561 mine $\mathcal{S}_{\mathcal{R}}$ the Rouse profile was integrated by approximating it as a series sum, which is
562 discussed in Appendix A in detail. The resultant shape factor reads

$$\mathcal{S}_{\mathcal{R}} = \left(\frac{h - z_o}{z_o}\right)^{\mathcal{R}} \left(\frac{\mathcal{R}^2 - 3\mathcal{R} + 2}{\mathcal{R}^2 - 2\mathcal{R} + 2}.\right) \tag{34}$$

563 One can infer from the above equation that when $\mathcal{R} \to 0$, the shape factor recov-
564 ers to 1, which is the shape factor for uniform sediment concentration. Increasing Rouse
565 number will increase the shape factor mainly because of the first multiplicative term in
566 parenthesis on the right-hand side of Equation 34. For discussion on the accuracy of the
567 second-order approximation, the reader is referred to Appendix A.

568 Similarly, the shape factor of the modified Rouse profile in the following equation
569 is obtained after integrating the modified Rouse profile by approximating the concen-
570 tration profile as a series sum (see Appendix B for detailed derivation):

$$\mathcal{S} = \left(\frac{h}{h - z_o}\right)^{\mathcal{R}\mathcal{M}} \left[\frac{\mathcal{R}^2 - 3\mathcal{R} + 2}{(\mathcal{M}+1)\mathcal{R}^2 - (\mathcal{M}+2)\mathcal{R} + 2}\right]. \tag{35}$$

571 The ratio between the shape factors of the modified and non-modified Rouse pro-
572 files, that is, $\mathcal{S}/\mathcal{S}_{\mathcal{R}}$, finds f after straightforward algebraic steps:

$$f(\mathcal{R},\mathcal{M}) = \left(\frac{h}{h-z_o}\right)^{-\mathcal{R}\mathcal{M}} \left(1-\mathcal{M}\frac{\mathcal{R}^2-\mathcal{R}}{\mathcal{R}^2-2\mathcal{R}+2}\right)^{-1}. \tag{36}$$

573 The reference height can be considered negligibly small relative to the flow depth,
574 so that $h - z_o \approx h$, making the first multiplicative term on the right-hand side one.
575 With this simplification, Equation 36 is further reduced to

$$f(\mathcal{R},\mathcal{M}) = \left(1-\mathcal{M}\frac{\mathcal{R}^2-\mathcal{R}}{\mathcal{R}^2-2\mathcal{R}+2}\right)^{-1}. \tag{37}$$

576 In the low settling velocity limit, the second term within the parenthesis approaches
577 zero, that is

$$\mathcal{M}\frac{\mathcal{R}^2-\mathcal{R}}{\mathcal{R}^2-2\mathcal{R}+2} \to 0. \tag{38}$$

578 In this limit, $f(\mathcal{R},\mathcal{M})$ can be approximated to

$$f(\mathcal{R},\mathcal{M}) = 1+\mathcal{M}\frac{\mathcal{R}^2-\mathcal{R}}{\mathcal{R}^2-2\mathcal{R}+2}. \tag{39}$$

579 Referring to the definition of $\mathcal{M}$ (see Equation 17) and after a few algebraic steps,
580 we obtained the following as the shape factor

$$\mathcal{S} = \mathcal{S}_{\mathcal{R}} + \mathcal{G}(\mathcal{R})\langle c\rangle, \tag{40}$$

581 where

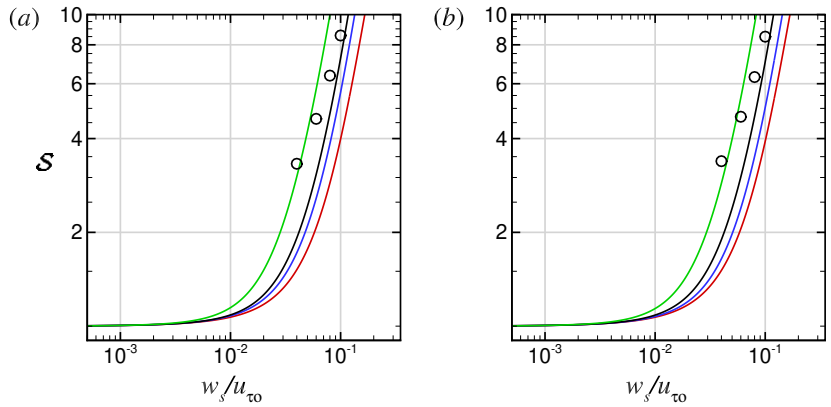

Figure 6: Comparison of the shape factors obtained from the simulations (hollow circles) and those obtained from Equation 40 (solid curves) for (a) $\sin\theta = 0.005$ and (b) $\sin\theta = 0.005$. Curves in red, blue, black, and green in both panels are obtained by using the respective values of S_c and $\mathcal{M}$ from A1-5 and B1-5.

$$\mathcal{G}(\mathcal{R}) = \left[\frac{\alpha(s-1)gh}{u_{\tau o}^2}\right]\mathcal{R}^2\mathcal{S}_{\mathcal{R}}. \tag{41}$$

The shape factor obtained from Equation 40 is compared with those obtained from the simulations in Figure 6. We used the depth-averaged concentration to obtain the Monin-Obukhov parameter in the simulations. Equations 40 and 41 estimate the shape factor of the simulated cases, suggesting that the assumption to obtain the shape factor are reasonable and can be faithfully used. Referring to Equation 22 and the definition of the densimetric Froude number (see Equation 25), one can obtain the deposition flux as follows

$$\left(\frac{w_s}{u_{\tau o}}\right)\mathcal{S}\langle c\rangle = (\kappa S_c\mathcal{R})\,\mathcal{S}_{\mathcal{R}}\left[\langle c\rangle + \alpha\left(\frac{\mathcal{R}}{Fr_o}\right)^2\langle c\rangle^2\right]. \tag{42}$$

From the quadratic dependence of settling flux on depth-averaged sediment concentration, the nonlinearity in the settling flux induced by density stratification can clearly be inferred. With the settling and erosion fluxes at hand, the depth-integrated dynamic equation of sediment concentration becomes

$$\frac{1}{u_{\tau o}}\frac{d\langle c\rangle h}{dt} = \left(\frac{m_e}{u_{\tau o}}\right)\xi - (\kappa S_c \mathcal{R})\mathcal{S}_{\mathcal{R}}\langle c\rangle + \left[\left(\frac{m_e}{u_{\tau o}}\right)\left(\frac{1+\xi}{2}\right)\left(\frac{\sin\theta}{Fr_o^2}\right)^2 - (\alpha\kappa S_c)\left(\frac{\mathcal{R}^3\mathcal{S}_{\mathcal{R}}}{Fr_o^2}\right)\right]\langle c\rangle^2. \tag{43}$$

The rightmost term in Equation 43 accounts for the nonlinear effects of density stratification and the cross-shelf gravity force as an explicit function of the depth-integrated concentration $\langle c\rangle$. The implications of Equation 43 will be discussed in the following subsection.

4.3 Applications

From the dynamic depth-integrated sediment concentration equation, one can infer that the right-hand side of Equation 43 must have real root(s) for equilibrium to establish. When the coefficient in front of the second-order term on the right-hand side is positive and there is no sediment suspension initially, the growth in sediment suspension will cease when $\langle c\rangle$ reaches the smaller root (see Figure 7a for graphical description). If the coefficient in front of the second-order term on the right-hand side of Equation 43 is negative, equilibrium will be established around the only positive root (see Figure 7b). Note that the lower root is inherently negative in the latter case. Around the equilibrium concentration, any small change in concentration will be forced to return back to the equilibrium concentration.

Equation 43 allows us to determine the parametric relation that marks the transition of ACSTCs to self-driven turbidity currents. In addition, the depth-averaged concentration of ACSTCs under equilibrium conditions can also be determined by using Equation 43. In the following two subsections, we will respectively discuss the relations for stability and suspended sediment load.

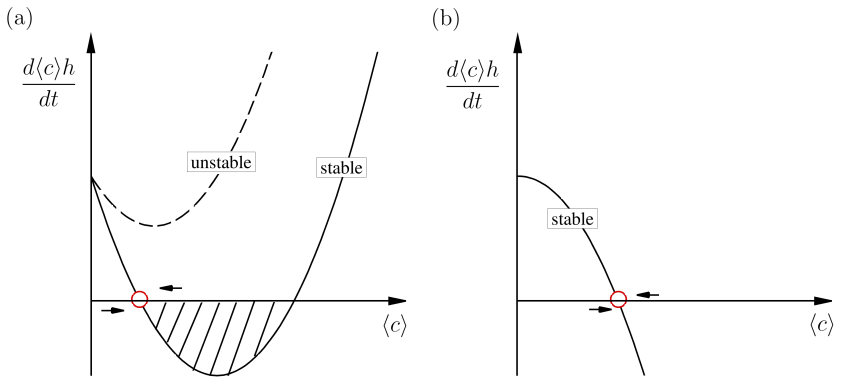

Figure 7: Descriptive sketch for the stability of the dynamic depth-integrated concentration equation for (a) $\alpha\kappa\left(\frac{\mathcal{R}^2\mathcal{F}(\mathcal{R})}{Fr_o^2}\right) > \left(\frac{m_e}{u_{\tau o}}\right)\left(\frac{1+\xi}{2}\right)\left(\frac{\sin\theta}{Fr_o^2}\right)^2$ (b) $\alpha\kappa\left(\frac{\mathcal{R}^2\mathcal{F}(\mathcal{R})}{Fr_o^2}\right) < \left(\frac{m_e}{u_{\tau o}}\right)\left(\frac{1+\xi}{2}\right)\left(\frac{\sin\theta}{Fr_o^2}\right)^2$. Condition in (a) makes the right-hand side of Equation 43 a convex curve, which may or may not have a real root. The condition in (b) makes the flow stable because the right-hand side of Equation 43 is a concave curve, which has a positive root.

4.3.1 Stability Conditions for ACSTCs and Turbidity Current Trigger

For the right-hand side of Equation 43 to have real roots, its discriminant must be positive, which leads to the following inequality after straightforward algebraic steps

$$(\kappa S_c \mathcal{R}\mathcal{S}_\mathcal{R})^2 + 4\alpha\kappa S_c\,\xi\left(\frac{m_e}{u_{\tau o}}\right)\frac{\mathcal{R}^3\mathcal{S}_\mathcal{R}}{Fr_o^2} > 2\xi(1+\xi)\left(\frac{m_e}{u_{\tau o}}\right)^2\left(\frac{\sin\theta}{Fr_o^2}\right)^2. \tag{44}$$

For a better physical interpretation, Equation 44 is divided by $(w_s/u_{\tau o})^2$, or $(\kappa S_c\mathcal{R})^2$, which reads

$$\underbrace{\mathcal{S}_\mathcal{R}^2}_{I} + \underbrace{4\alpha\xi\left(\frac{m_e}{w_s}\right)\frac{\mathcal{R}^2\mathcal{S}_\mathcal{R}}{Fr_o^2}}_{II} > \underbrace{2\xi(1+\xi)\left(\frac{m_e}{w_s}\right)^2\left(\frac{\sin\theta}{Fr_o^2}\right)^2}_{III} \tag{45}$$

Equation 45 has three terms, denoted as I, II, and III, which are associated with different physical mechanisms. The first term solely depends on the Rouse profile's shape factor, that is $\mathcal{S}_\mathcal{R}$. Because increasing sediment size or w_s reduces sediment suspension

in a Rousean profile, term I can be considered as resistance to suspension due to a stronger settling effect. With increasing w_s sediments tend to deposit, creating a favorable condition for stability. It must be noted that this term is dissociated from density stratification because it would be present even in the absence of density stratification. Dissociation of term I from density stratification can be inferred from its dependence on the shape factor of the Rouse profile because the Rouse profile does not consider any turbulence dissipation due to density stratification.

The second term, that is term II, is associated with the stabilizing effect of density stratification. Although it has a stabilizing effect on ACSTCs, this term includes m_e and ξ, which govern the entrainment from the bed, which also creates a higher downslope gravity force. This may appear counter-intuitive at first, but the following offers an explanation. The amount of sediments entrained, which is quantified through $m_e\xi$, will enhance the density stratification -quantified by the product of $m_e\xi$ and Fr_o^{-2}- changes the shape of the concentration profile through $\alpha\mathcal{R}^3\mathcal{S}_{\mathcal{R}}Fr_o^{-2}$, and thus resist suspension. Finally, the third term mathematically describes the potential of entrainment growth due to cross-shelf gravity force.

The stability condition in Equation 45 is compared with the simulation results. In the numerical simulations, w_s and $\sin\theta$ were varied while the other terms were kept constant. Therefore, we plot I+II-III against $w_s/u_{\tau o}$ in Figure 7, where its intercept locates the critical settling velocity for (in)stability. The critical settling velocity is found as $w_s/u_{\tau o} = 0.024$ for $\sin\theta = 0.01$. The critical settling velocity falls between $w_s/u_{\tau o} = 0.02$ and $w_s/u_{\tau o} = 0.04$, which are respectively the unstable and stable cases in the simulations conducted for $\sin\theta = 0.01$. Albeit limited in number, the simulations support Equation 45's capability to delineate the stable and unstable conditions for ACSTCs.

The magnitudes of each term provide information as to the dominant mechanisms that (de)stabilize ACSTCs. To this end, Figure 9 plots the absolute values of terms I, II, and III against $w_s/u_{\tau o}$. From figure 9, one can observe that especially when $w_s/u_{\tau o} \rightarrow$

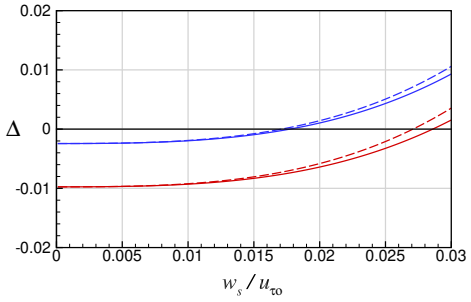

Figure 8: Variation of Δ = I+II-III with respect to $w_s/u_{\tau o}$. Curves in blue and red respectively indicate $\sin\theta = 0.005$ and $\sin\theta = 0.01$. Solid and dashed curves indicate the minimum and the maximum values of Δ from different α and S_c combinations listed in Table 2

0, term III becomes dominant and results in instability. In this limit, the magnitude of terms I and II are substantially lower than that of term III (see Figure 9a), and the magnitude of term I is larger than that of term II for $w_s/u_{\tau o} < 0.002$ (see Figure 3b). However, the growth rate of term II with respect to $w_s/u_{\tau o}$ is significantly larger than that of term I, and its magnitude becomes an order of term I's magnitude, suggesting that density stratification becomes the dominant mechanism to maintaining ACSTCs, especially for $w_s/u_{\tau o} > 0.01$. It is worth reiterating that density stratification is a function of the entrainment parameters because the amount of entrained sediments controls the amount of sediment suspension, and the amount of sediment suspension governs the density stratification. Referring to the gradient Richardson number profiles, one should note that the dominant role of sediment-induced density stratification does not warrant a critically stratified condition. Density stratification may impose control on the sediment suspension even under subsaturated conditions.

4.3.2 Estimation of Depth-averaged Sediment Concentration

For the specified problem herein, in which there is no initial sediment suspension, depth-averaged concentration will equilibrate at the smaller root of Equation 43's right-hand side. Equilibrium concentration will therefore read

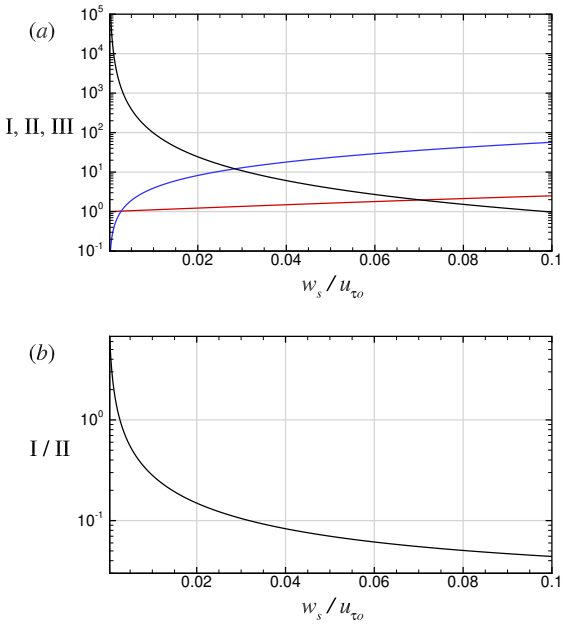

Figure 9: (a) Magnitude of terms I, II, and III for Case A4. Note that Terms I and II are independent of $\sin\theta$ while III is linearly proportional to $\sin\theta$. (b)Variation of the ratio between the destabilizing terms due to settling and density stratification that is I/II, with respect to $w_s/u_{\tau o}$. Note in both subfigures that ξ, m_e, and Fr_o are taken as constants.

$$\langle c \rangle = \frac{Fr_o^2 - \sqrt{Fr_o^4 - 2\xi(1+\xi)\left(\frac{m_e}{\mathcal{S}_{\mathcal{R}} w_s}\sin\theta\right)^2 + 4\alpha\xi\left(\frac{m_e}{\mathcal{S}_{\mathcal{R}} w_s}\right)(\mathcal{R}\, Fr_o)^2}}{(1+\xi)\left(\frac{m_e}{\mathcal{S}_{\mathcal{R}} w_s}\right)\left(\frac{\sin\theta}{Fr_o}\right)^2 - 2\alpha\mathcal{R}^2}. \tag{46}$$

Depth-averaged concentration estimate from Equation 46 is plotted in Figure 10 with respect to $w_s/u_{\tau o}$ and compared with the amount of sediment suspension obtained from the simulations. The solid and the dashed curves plotted in the same figure respectively indicate the depth-averaged sediment concentration obtained by using the S_c and $\mathcal{M}$ combinations that gives the smallest and the largest sediment concentration. There is a close match between the sediment suspension amount estimated by Equation 46 and those obtained from the simulations. Noting that the depth-averaged sediment concentration depends on entrainment parameters, sediment settling velocity (or the Rouse number), cross-shelf bed gradient, and α, the amount of sediment suspension cannot simply be estimated by a critical Richardson number. This is true even though the amount of

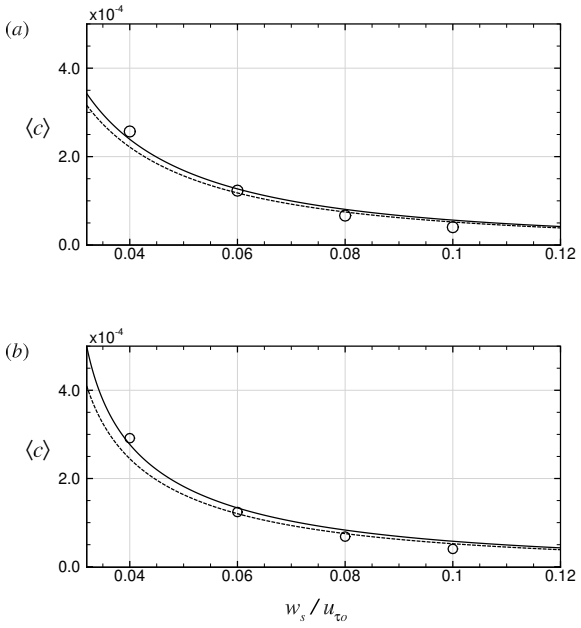

Figure 10: Comparison between the estimated (Equation 46) and observed (hollow circles)volumetric suspended sediment concentration from the simulations for (a) $\sin\theta = 0.005$ and (b) $\sin\theta = 0.01$. Solid and dashed curves indicate the maximum and the minimum concentration obtained from different α and S_c combinations listed in Table 2.

suspension in ACSTCs is controlled by density stratification, which can be inferred from the stability condition in Equation 45 in that density stratification is controlled by both the settling velocity and the amount of suspension. And the amount of sediment suspension is governed by the erosion parameters along with the settling velocity and the strength of the bed shear stress. On the other hand, the bulk Richardson number considers only the amount of sediment suspension, the velocity of the alongshelf current, and the cross-shelf velocity of ACSTCs.

5 Conclusions

In this study, an analytical dynamic depth-integrated concentration equation was developed for ACSTCs. The model developed accounts for the non-linearity associated with the positive feedback loop between the sediment entrainment and the cross-shelf gravity force, as well as the sediment-induced density stratification. These non-linear mech-

anisms are approximated as explicit quadratic functions of depth-averaged suspended sediment concentration ($\langle c \rangle$). From the model developed, a quantitative relation for the critical conditions for the trigger of a self-driven turbidity current that grows out of an ACSTC is developed. It is found that the critical condition for self-driven turbidity current trigger depends on the parameters that help grow the amount of sediment suspension. These parameters include the cross-shelf bed gradient, sediment entrainment parameters, m_e and ξ, settling velocity, or the shape factor for the Rouse profile ($\mathcal{S}_{\mathcal{R}}$), and the parameters associated with sediment-induced density stratification.

The two stabilizing terms and one destabilizing term in Equation 45, which finds the critical conditions for the trigger, provide information regarding the governing physical processes in ACSTCs. The destabilizing term, namely term III, quantifies the positive feedback loop between the sediment entrainment and the cross-shelf gravity force and is a function of the cross-shelf bed slope, ease of entrainment m_e/w_s and normalized excess shear stress due to alongshelf current ξ. The first stabilizing term, that is term I, is the sediment settling flux, independent of sediment-induced density stratification. The second stabilizing term quantifies sediment-induced density stratification effect on the amount of sediment suspension, which is a function of α, sediment settling velocity, and entrainment parameters, which are sediment entrainment rate m_e and normalized excess shear stress due to alongshelf current ξ. The magnitude of term II, which quantifies density stratification, relative to that of term I, which quantifies mere settling, is substantially larger for the most part except when $w_s \to 0$. In this limit, density stratification almost vanishes, making the mere settling term the only stabilizing mechanism. However, with increasing $w_s/u_{\tau o}$, term II sharply increases and outgrows term I. Therefore, it is concluded that density stratification is the dominant mechanism to maintain ACSTCs.

The amount of depth-averaged sediment concentration found in Equation 46 is a function of settling velocity, excess shear stress, and sediment entrainment parameters.

This finding suggests that the depth-averaged concentration is governed by the balance of sediment entrainment, density stratification, and mere settling. Bulk Richardson number showed a five-fold change in the simulations without reaching a global constant value. Furthermore, in all the simulated ACSTCs, the gradient Richardson number profiles do not collapse onto a single curve, suggesting that critical density stratification does not regulate sediment entrainment and deposition, and critical density stratification is not a necessary condition for ACSTCs.All the findings suggest that depth-integrated suspended sediment concentration and the critical conditions for the turbidity current generation out of ACSTCs are regulated by the density stratification, sediment entrainment, including its nonlinear interaction with the downslope gravity force, and deposition. All these findings provide evidence to our hypotheses in Section 1.3.

Appendix A Derivation of the Rouse Profile's Shape Factor

The shape factor for the Rouse profile $\mathcal{S}_{\mathcal{R}}$ is the ratio between the sediment concentration at the bed and the depth-averaged concentration. To integrate the Rouse profile conveniently, it will be expressed in dimensionless form, where the distance from the bed is normalized by the depth, that is $\tilde{z} = z/h$. The dimensionless Rouse profile reads

$$c = c_o \left(\frac{\tilde{z}_o}{1 - \tilde{z}_o} \right)^{\mathcal{R}} \tilde{z}^{-\mathcal{R}} \left(1 - \tilde{z}\right)^{\mathcal{R}}, \tag{A1}$$

where $\tilde{z}_o = z_o/h$. The integration of the dimensionless Rouse profile yields the depth-averaged concentration $\langle c \rangle$

$$\int_{\tilde{z}=\tilde{z}_o}^{\tilde{z}=1} c(\tilde{z}) d\tilde{z} = h^{-1} \int_{z=z_o}^{z=h} c(z) dz \tag{A2}$$

because $dz = h d\tilde{z}$. To analytically obtain the shape factor, $(1-\tilde{z})^{\mathcal{R}}$ is expanded as a binomial series

$$(1-\tilde{z})^{\mathcal{R}} = 1 - \mathcal{R}\tilde{z} + \mathcal{R}(\mathcal{R}-1)\frac{\tilde{z}^2}{2} - \mathcal{R}(\mathcal{R}-1)(\mathcal{R}-2)\frac{\tilde{z}^3}{6} + \dots . \tag{A3}$$

Thus,

$$\tilde{z}^{-\mathcal{R}}(1-\tilde{z})^{\mathcal{R}} = \tilde{z}^{-\mathcal{R}} - \mathcal{R}\tilde{z}^{1-\mathcal{R}} + \mathcal{R}(\mathcal{R}-1)\frac{\tilde{z}^{2-\mathcal{R}}}{2} - \mathcal{R}(\mathcal{R}-1)(\mathcal{R}-2)\frac{\tilde{z}^{3-\mathcal{R}}}{6} + \dots . \tag{A4}$$

By utilizing Equation A4, the Rouse profile can be written as

$$c(\tilde{z}) = c_o \left(\frac{\tilde{z}_o}{1-\tilde{z}_o}\right)^{\mathcal{R}} \left[\tilde{z}^{-\mathcal{R}} - \mathcal{R}\tilde{z}^{1-\mathcal{R}} + \mathcal{R}(\mathcal{R}-1)\frac{\tilde{z}^{2-\mathcal{R}}}{2} - \mathcal{R}(\mathcal{R}-1)(\mathcal{R}-2)\frac{\tilde{z}^{3-\mathcal{R}}}{6} + \dots\right] \tag{A5}$$

First-, second-, and third-order approximations are compared with the actual Rouse profiles for $w_s/u_{\tau o} = 0.04$ and 0.10 in Figure A1. Past the first order, approximated concentration profiles are close to one another. For the settling velocities selected, serial approximation follows the actual Rouse profile. The error mainly occurs close to the top boundary where there is a sharp concentration gradient. Integration of Equation A5 will result in

$$\int c(\tilde{z})d\tilde{z} = c_o \left(\frac{\tilde{z}_o}{1-\tilde{z}_o}\right)^{\mathcal{R}} \left[\frac{1}{1-\mathcal{R}}\tilde{z}^{1-\mathcal{R}} - \frac{\mathcal{R}}{2-\mathcal{R}}\tilde{z}^{2-\mathcal{R}} + \frac{\mathcal{R}(\mathcal{R}-1)}{2(3-\mathcal{R})}\tilde{z}^{3-\mathcal{R}} - \dots\right] + \mathcal{A} \tag{A6}$$

where $\mathcal{A}$ is the constant of integration. Since $z_o/h = \tilde{z} \approx 0$, the lower bound of the integral can be neglected. Approximating the term within the brackets up to the second-order, that is $\mathcal{O}(\tilde{z}^2)$, the integral of the Rouse profile is obtained as

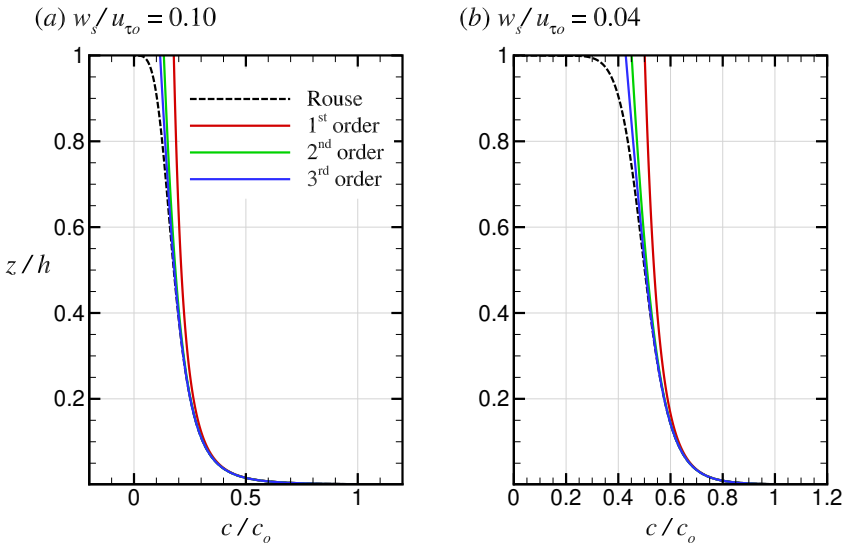

Figure A1: Comparison of the first- (red), second- (green), and third-order (blue) approximations of the Rouse profile with the actual Rouse profile (dashed curve) for (a) $w_s/u_{\tau o} = 0.10$ and (b) $w_s/u_{\tau o} = 0.04$. Note that the concentration profiles are normalized by the reference concentration c_o and becomes unity at the reference height z_o.

$$\int_{\tilde{z}=\tilde{z}_o}^{\tilde{z}=1} c(\tilde{z})d\tilde{z} = c_o \left(\frac{\tilde{z}_o}{1-\tilde{z}_o}\right)^{\mathcal{R}} \left(\frac{\mathcal{R}^2 - 2\mathcal{R} + 2}{\mathcal{R}^2 - 3\mathcal{R} + 2}\right) \tag{A7}$$

By approximating the sediment concentration at the bed to the reference concentration, that is $c_b \approx c_o$, the shape factor for the Rouse profile will be obtained as

$$\mathcal{S}_{\mathcal{R}} = \frac{c_o}{\int_{\tilde{z}=\tilde{z}_o}^{\tilde{z}=1} c(\tilde{z})d\tilde{z}} = \left(\frac{h-z_o}{z_o}\right)^{\mathcal{R}} \left(\frac{\mathcal{R}^2 - 3\mathcal{R} + 2}{\mathcal{R}^2 - 2\mathcal{R} + 2}\right) \tag{A8}$$

Appendix B Derivation of the Modified Rouse Profile's Shape Factor

The shape factor for the modified Rouse profile $\mathcal{S}$ is determined similar to that for the Rouse profile. The dimensionless modified Rouse profile reads

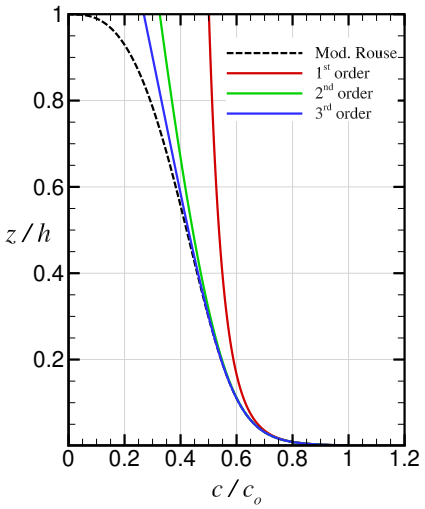

Figure B1: Comparison of the first- (red), second- (green), and third-order (blue) approximations of the modified Rouse profile with the actual modified Rouse profile (dashed curve) for $w_s/u_{\tau o} = 0.04$. The Monin-Obukhov parameter $\mathcal{M} = 25$. Various values of $\mathcal{M}$ are also tested and similar results are obtained; therefore, only the profiles from $\mathcal{M} = 25$ is shown for brevity. Note that the concentration profiles are normalized by the reference concentration c_o and becomes unity at the reference height z_o.

$$c = c_o \left[\frac{\tilde{z}_o^{\mathcal{R}}}{(1-\tilde{z}_o)^{\mathcal{R}(\mathcal{M}+1)}} \right] \tilde{z}^{-\mathcal{R}} (1-\tilde{z})^{\mathcal{R}(\mathcal{M}+1)} \tag{B1}$$

After expanding $(1-\tilde{z})^{\mathcal{R}\mathcal{M}+\mathcal{R}}$ as binomial series similar to that for the Rouse profile, $\tilde{z}^{-\mathcal{R}}(1-\tilde{z})^{\mathcal{R}\mathcal{M}+\mathcal{R}}$ is obtained as

$$\begin{aligned} \tilde{z}^{-\mathcal{R}}(1-\tilde{z})^{\mathcal{R}\mathcal{M}+\mathcal{R}} = \tilde{z}^{-\mathcal{R}} - (\mathcal{R}\mathcal{M}+\mathcal{R})\tilde{z}^{1-\mathcal{R}} + (\mathcal{R}\mathcal{M}+\mathcal{R}-1)(\mathcal{R}\mathcal{M}+\mathcal{R})\frac{\tilde{z}^{2-\mathcal{R}}}{2} \\ -(\mathcal{R}\mathcal{M}+\mathcal{R}-2)(\mathcal{R}\mathcal{M}+\mathcal{R}-1)(\mathcal{R}\mathcal{M}+\mathcal{R})\frac{\tilde{z}^{3-\mathcal{R}}}{6} + ... \end{aligned} \tag{B2}$$

Using Equation B2, the modified Rouse profile is then obtained as

$$c(\tilde{z}) = c_o \frac{\tilde{z}_o^{\mathcal{R}}}{(1-\tilde{z}_o)^{\mathcal{R}(\mathcal{M}+1)}} \left[\tilde{z}^{-\mathcal{R}} - (\mathcal{R}\mathcal{M}+\mathcal{R})\tilde{z}^{1-\mathcal{R}} + (\mathcal{R}\mathcal{M}+\mathcal{R}-1)(\mathcal{R}\mathcal{M}+\mathcal{R})\frac{\tilde{z}^{2-\mathcal{R}}}{2} - ... \right] \tag{B3}$$

Approximated concentration profiles are shown for the first, second, and the third orders in Figure B1. From the same figure, one can observe that increasing order of approximation improves the accuracy, but the difference between the second- and the third-order approximations is small. Therefore, we will use the second-order approximation henceforth. For the second-order approximation, the integral of the concentration profile becomes

$$\int c(\tilde{z})d\tilde{z} = c_o \frac{\tilde{z}_o^{\mathcal{R}}}{(1-\tilde{z}_o)^{\mathcal{R}\mathcal{M}}} \tilde{z}^{-\mathcal{R}} \left[\frac{1}{1-\mathcal{R}}\tilde{z} - \frac{\mathcal{R}\mathcal{M}+\mathcal{R}}{2-\mathcal{R}}\tilde{z}^2 + \frac{(\mathcal{R}\mathcal{M}+\mathcal{R})(\mathcal{R}\mathcal{M}+\mathcal{R}-1)}{2(3-\mathcal{R})}\tilde{z}^3 - ... \right] + \mathcal{B} \tag{B4}$$

where $\mathcal{B}$ is the constant of integration. Since $z_o/h \approx 0$, the lower bound of the integral can be neglected. Keeping the terms up to the second-order, that is $\mathcal{O}(\tilde{z}^2)$, the integral of the Rouse profile is obtained as

$$\int_{\tilde{z}=\tilde{z}_o}^{\tilde{z}=1} c(\tilde{z})d\tilde{z} = c_o \frac{\tilde{z}_o^{\mathcal{R}}}{(1-\tilde{z}_o)^{\mathcal{R}\mathcal{M}+\mathcal{R}}} \left[\frac{(\mathcal{M}+1)\mathcal{R}^2 - (\mathcal{M}+2)\mathcal{R}+2}{\mathcal{R}^2-3\mathcal{R}+2} \right] \tag{B5}$$

From the depth-averaged concentration, the shape factor for the modified Rouse profile will be obtained as

$$\mathcal{S} = \frac{c_o}{\int_{\tilde{z}=\tilde{z}_o}^{\tilde{z}=1} c(\tilde{z})d\tilde{z}} = \left(\frac{z_o}{h-z_o}\right)^{\mathcal{R}} \left(\frac{h}{h-z_o}\right)^{\mathcal{R}\mathcal{M}} \left[\frac{\mathcal{R}^2-3\mathcal{R}+2}{(\mathcal{M}+1)\mathcal{R}^2-(\mathcal{M}+2)\mathcal{R}+2} \right] \tag{B6}$$

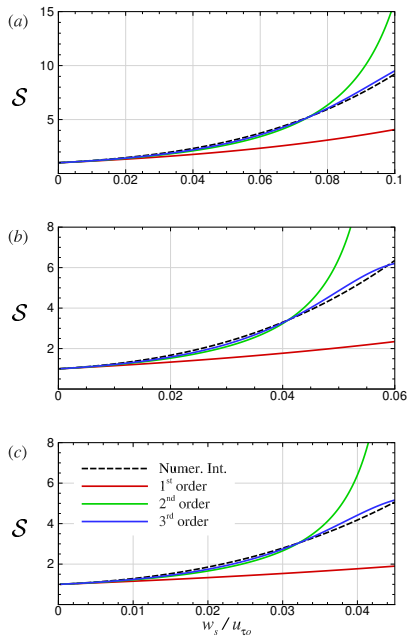

Figure B2: Comparison of the the modified Rouse profile's first, second, and third-order approximations with those obtained from the numerical integration of the modified Rouse profile. The Monin-Obukhov paramater is $\mathcal{M} = 25$ in (a), $\mathcal{M} = 90$ in (b), and $\mathcal{M} = 150$ in (c).

The shape factor obtained is also compared with its first- and third-order order counterpart as well as the shape factor obtained after numerically integrating the modified Rouse profile (see Figure B2). The second- and the third-order approximations are close to the numerically integrated shape factor from $w_s/u_{\tau o} = 0$ to $w_s/u_{\tau o} = 0.80$, $w_s/u_{\tau o} = 0.45$, and $w_s/u_{\tau o} = 0.34$ for $\mathcal{M} = 25$, $\mathcal{M} = 90$, and $\mathcal{M} = 150$, respectively. Therefore, the settling velocity range where second-order approximation holds narrows with increasing $\mathcal{M}$. This is also true for the third-order approximation, but the range of applicability for the third-order approximation is slightly larger than the second-order approximation. However, it must be noted that the given analysis is conducted for *a priori* $\mathcal{M}$ value. On the other hand, the suspended sediment load, hence the Monin-Obukhov parameter $\mathcal{M}$, decreases with increasing settling velocity where sediments are sourced from the bed. As such, second- and third-order approximations still remain applicable for increasing settling velocity.

Data Availability

The source code and case setup to reproduce the results and the mean quantities that produced the figures are publicly available in open science framework at https://doi.org/10.17605/OSF.IO/8BKXR.

Acknowledgments

Funding for this study was provided by NSF (OCE-20203676). High-performance computational resources provided by Louisiana State University (http://www.hpc.lsu.edu) are greatly acknowledged. The majority of the simulations for this study were conducted as a part of the course entitled "High-performance Computing Applications in Environmental Flows" offered by the first author. Ms. Sahar Haddadian is acknowledged for conducting the preliminary simulations, whose results inspired this study.

References

Ayranci, K., Lintern, D. G., Hill, P. R., & Dashtgard, S. E. (2012). Tide-supported gravity flows on the upper delta front, Fraser River delta, Canada. *Marine Geology*, *326*, 166–170.

Bhattacharya, J. P., Copeland, P., Lawton, T. F., & Holbrook, J. (2016). Estimation of source area, river paleo-discharge, paleoslope, and sediment budgets of linked deep-time depositional systems and implications for hydrocarbon potential. *Earth-Science Reviews*, *153*, 77–110.

Cantero, M. I., Balachandar, S., & Garcia, M. H. (2008). An Eulerian–Eulerian model for gravity currents driven by inertial particles. *International Journal of Multiphase Flow*, *34*(5), 484–501.

Cantero, M. I., Shringarpure, M., & Balachandar, S. (2012). Towards a universal criteria for turbulence suppression in dilute turbidity currents with non-cohesive sediments. *Geophysical Research Letters*, *39*(14).

Cellino, M., & Graf, W. H. (1999). Sediment-laden flow in open-channels under noncapacity and capacity conditions. *Journal of Hydraulic Engineering*, *125*, 455-462.

Cheng, Z., Yu, X., Hsu, T.-J., Ozdemir, C. E., & Balachandar, S. (2015). On the transport modes of fine sediment in the wave boundary layer due to resuspension/deposition: A turbulence-resolving numerical investigation. *Journal of Geophysical Research: Oceans*, *120*(3), 1918–1936.

Chorin, A. J. (1968). Numerical solution of the navier-stokes equations. *Mathematics of Computation*, *22*(104), 745–762.

Cortese, T. A., & Balachandar, S. (1995). High performance spectral simulation of turbulent flows in massively parallel machines with distributed memory. *The International Journal of Supercomputer Applications and High Performance Computing*, *9*(3), 187–204.

Curran, K., Hill, P., Milligan, T., Mikkelsen, O., Law, B., de Madron, X. D., & Bourrin, F. (2007). Settling velocity, effective density, and mass composition of suspended sediment in a coastal bottom boundary layer, Gulf of Lions, France. *Continental Shelf Research*, *27*(10-11), 1408–1421.

Denommee, K. C., Bentley, S. J., Harazim, D., & Macquaker, J. H. (2016). Hydrodynamic controls on muddy sedimentary-fabric development on the Southwest Louisiana subaqueous delta. *Marine Geology*, *382*, 162–175.

Fain, A., Ogston, A., & Sternberg, R. (2007). Sediment transport event analysis on the western Adriatic continental shelf. *Continental Shelf Research*, *27*(3-4), 431–451.

Flores, R. P., Rijnsburger, S., Meirelles, S., Horner-Devine, A. R., Souza, A. J., Pietrzak, J. D., ... Reniers, A. (2018). Wave generation of gravity-driven sediment flows on a predominantly sandy seabed. *Geophysical Research Letters*, *45*(15), 7634–7645.

Haddadian, S., Ozdemir, C., Goodlow, B., Xue, G., & Bentley, S. (2021). Direct

numerical simulations of miniature along-shelf current-supported turbidity currents: Conceptual investigation of velocity structure and drag coefficient. *Journal of Geophysical Research: Oceans*, *126*(8), e2020JC016736.

Hale, R. P., & Ogston, A. S. (2015). In situ observations of wave-supported fluid-mud generation and deposition on an active continental margin. *Journal of Geophysical Research: Earth Surface*, *120*(11), 2357–2373.

Hooshmand, A., Horner-Devine, A. R., & Lamb, M. P. (2015). Structure of turbulence and sediment stratification in wave-supported mud layers. *Journal of Geophysical Research: Oceans*, *120*(4), 2430–2448.

Itakura, T., & Kishi, T. (1980). Open channel flow with suspended sediments. *Journal of Hydraulics Division*, *106*(8), 1325–1343.

Jaramillo, S., Sheremet, A., Allison, M., Reed, A., & Holland, K. (2009). Wave-mud interactions over the muddy Atchafalaya subaqueous clinoform, Louisiana, United States: Wave-supported sediment transport. *Journal of Geophysical Research: Oceans*, *114*(C4).

Komar, P. D. (1977). Computer simulation of turbidity current flow and the study of deep-sea channels and fan sedimentation. In E. Goldberg, I. McCave, J. O'Brian, & S. J.H. (Eds.), *Marine Modeling (The Sea)* (Vol. 6, p. 603-621). New York: Wiley.

Ma, Y., Friedrichs, C. T., Harris, C. K., & Wright, L. D. (2010). Deposition by seasonal wave-and current-supported sediment gravity flows interacting with spatially varying bathymetry: Waiapu shelf, New Zealand. *Marine Geology*, *275*(1-4), 199–211.

Ma, Y., Wright, L. D., & Friedrichs, C. T. (2008). Observations of sediment transport on the continental shelf off the mouth of the Waiapu River, New Zealand: Evidence for current-supported gravity flows. *Continental Shelf Research*, *28*(4), 516-532. doi: https://doi.org/10.1016/j.csr.2007.11.001

Macquaker, J. H., Bentley, S. J., & Bohacs, K. M. (2010). Wave-enhanced sediment-

gravity flows and mud dispersal across continental shelves: Reappraising sediment transport processes operating in ancient mudstone successions. *Geology*, *38*(10), 947–950.

Martin, D., Nittrouer, C., Ogston, A., & Crockett, J. (2008). Tidal and seasonal dynamics of a muddy inner shelf environment, Gulf of Papua. *Journal of Geophysical Research: Earth Surface*, *113*(F1).

Monin, A. S., & Obukhov, A. M. (1954). Basic laws of turbulent mixing in the surface layer of the atmosphere. *Contributions to Geophysical Institute of Academy of Sciences USSR*, *151*(163), e187.

Ogston, A. S., Sternberg, R. W., Nittrouer, C. A., Martin, D. P., Goñi, M. A., & Crockett, J. S. (2008). Sediment delivery from the Fly River tidally dominated delta to the nearshore marine environment and the impact of El Nino. *Journal of Geophysical Research: Earth Surface*, *113*(F1).

Ozdemir, C. E., Hsu, T.-J., & Balachandar, S. (2011). A numerical investigation of lutocline dynamics and saturation of fine sediment in the oscillatory boundary layer. *Journal of Geophysical Research: Oceans*, *116*(C9).

Parker, G., Fukushima, Y., & Pantin, H. M. (1986). Self-accelerating turbidity currents. *Journal of Fluid Mechanics*, *171*, 145–181.

Parsons, J. D., Friedrichs, C. T., Traykovski, P. A., Mohrig, D., Imran, J., Syvitski, J. P., ... others (2007). The mechanics of marine sediment gravity flows. *Continental margin sedimentation: from sediment transport to sequence stratigraphy*, *37*, 275–334.

Peng, Y., Yu, Q., Du, Z., Wang, L., Wang, Y., & Gao, S. (2022). Gravity-driven sediment flows on the shallow sea floor of a muddy open coast. *Marine Geology*, *445*, 106759.

Sanford, L. P., & Maa, J. P.-Y. (2001). A unified erosion formulation for fine sediments. *Marine Geology*, *179*(1-2), 9–23.

Sequeiros, O. E., Bolla Pittaluga, M., Frascati, A., Pirmez, C., Masson, D. G.,

887 Weaver, P., ... Rimmer, J. G. (2019). How typhoons trigger turbidity currents in
888 submarine canyons. *Scientific reports*, *9*(1), 1–15.
889 Traykovski, P., Geyer, W., Irish, J., & Lynch, J. (2000). The role of wave-induced
890 density-driven fluid mud flows for cross-shelf transport on the eel river continental
891 shelf. *Continental Shelf Research*, *20*(16), 2113–2140.
892 Traykovski, P., Trowbridge, J., & Kineke, G. (2015). Mechanisms of surface wave
893 energy dissipation over a high-concentration sediment suspension. *Journal of Geo-*
894 *physical Research: Oceans*, *120*(3), 1638–1681.
895 Traykovski, P., Wiberg, P. L., & Geyer, W. R. (2007). Observations and model-
896 ing of wave-supported sediment gravity flows on the Po prodelta and comparison
897 to prior observations from the Eel shelf. *Continental Shelf Research*, *27*(3-4),
898 375–399.
899 van Kessel, T., & Kranenburg, C. (1996). Gravity current of fluid mud on sloping
900 bed. *Journal of Hydraulic Engineering*, *122*(12), 710–717.
901 Walsh, J. P., Nittrouer, C. A., Palinkas, C. M., Ogston, A. S., Sternberg, R. W., &
902 Brunskill, G. J. (2004). Clinoform mechanics in the Gulf of Papua, New Guinea.
903 *Continental Shelf Research*, *24*(19), 2487–2510.
904 Williamson, J. H. (1980). Low-storage Runge-Kutta schemes. *Journal of Computa-*
905 *tional Physics*, *35*(1), 48–56.
906 Winterwerp, J. C. (2001). Stratification effects by cohesive and noncohesive sedi-
907 ment. *Journal of Geophysical Research: Oceans*, *106*(C10), 22559–22574.
908 Winterwerp, J. C., Lely, M., & He, Q. (2009). Sediment-induced buoyancy destruc-
909 tion and drag reduction in estuaries. *Ocean Dynamics*, *59*(5), 781–791.
910 Wright, L., & Friedrichs, C. (2006). Gravity-driven sediment transport on continen-
911 tal shelves: A status report. *Continental Shelf Research*, *26*(17), 2092-2107. doi:
912 https://doi.org/10.1016/j.csr.2006.07.008
913 Wright, L., Friedrichs, C., Kim, S., & Scully, M. (2001). Effects of ambient cur-
914 rents and waves on gravity-driven sediment transport on continental shelves. *Ma-*

rine Geology, *175*(1), 25-45. doi: https://doi.org/10.1016/S0025-3227(01)00140-2

Yue, L., Cheng, Z., & Hsu, T.-J. (2019). Turbid: A turbulence-resolving numerical model for simulating bottom boundary layer and fine sediment transport.

Yue, L., Cheng, Z., & Hsu, T.-J. (2020). A turbulence-resolving numerical investigation of wave-supported gravity flows. *Journal of Geophysical Research: Oceans*, *125*(2), e2019JC015220.

Zang, Z., Xue, Z. G., Xu, K., Ozdemir, C. E., Chen, Q., Bentley, S. J., & Sahin, C. (2020). A numerical investigation of wave-supported gravity flow during cold fronts over the Atchafalaya shelf. *Journal of Geophysical Research: Oceans*, *125*(9), e2019JC015269.

Zhang, W., Cui, Y., Santos, A. I., & Hanebuth, T. J. (2016). Storm-driven bottom sediment transport on a high-energy narrow shelf (NW Iberia) and development of mud depocenters. *Journal of Geophysical Research: Oceans*, *121*(8), 5751–5772.